Utility of Copernicus-Based Inputs for Actual Evapotranspiration Modeling in Support of Sustainable Water Use in Agriculture

Radoslaw Guzinski, Hector Nieto, Juan Manuel Sánchez, Ramón López-Urrea, Dalenda Mahjoub Boujnah, and Gilles Boulet

***Abstract*—Quantifying spatial and temporal patterns of the actual evapotranspiration (ET) using Earth observation data can significantly contribute to the accurate and transparent monitoring of sustainable development goals (SDGs) target 6.4, which focuses on the increase of the water-use efficiency and sustainable freshwater withdrawals. Irrigated agriculture is by far the largest consumer of freshwater worldwide, and ET can serve as a direct proxy of crop water use. Various ongoing initiatives encourage the use of remote sensing data for the monitoring of SDG 6.4, including the WaPOR portal run by the Food and Agriculture Organization of the United Nations. However, none of these initiatives use Copernicus satellite and modeled data to the fullest extent. Copernicus provides operational high-quality data freely and openly, contains all the inputs required for ET modeling, and has long-term continuity and evolution plans, thus allowing for the establishment of baseline for SDG 6.4 and continuous monitoring in mid- and long term. In this study, we evaluate the utility of Copernicus data for this task with WaPOR products serving as a comparison benchmark. Thus, the modeled ET has to be able to accurately capture the field-scale activity at 10-day timesteps while also scaling to national coverage and providing consistent estimates at different spatial resolutions, ranging from tens to hundreds of meters. Results indicate that Copernicus-based ET can reach a correlation of 0.9, mean bias of 0.3 mm/day, and root-mean-square error of less than 1 mm/day when compared against the field lysimeter and eddy covariance measurements, and with proper approach, can achieve a better spatial-scale consistency than WaPOR data. This sets a path toward the Copernicus-based ET product and its use within the SDG monitoring and reporting.**

***Index Terms*—Copernicus, evapotranspiration (ET), irrigation, sustainable development goals (SDGs).**

Manuscript received June 29, 2021; revised September 6, 2021; accepted October 15, 2021. Date of publication October 26, 2021; date of current version November 19, 2021. This work was supported in part by the European Space Agency (ESA) through ET4FAO project. The work of R. López-Urrea was supported in part by the "Agencia Estatal de Investigación" project AGL2017-83738-C3-3-R, in part by the JCCM (Spain) project SBPLY/17/180501/000357, both with FEDER cofinancing, and in part by the European Commission with project "SUPROMED" under Grant GA-1813. The work of J. M. Sánchez was supported by H2020 EC project "REXUS" under Grant 101003632. The work of G. Boulet and D. M. Boujnah was supported by the Olive Institute in Tunisia, in part by NAILA International Laboratory, and in part by WaterWorks2017 FLUXMED and PRIMA 2018 ALTOS ERA-NET Cofund projects. *(Corresponding author: Radoslaw Guzinski.)*

Radoslaw Guzinski is with DHI GRAS, 2970 Hørsholm, Denmark (e-mail: rmgu@dhigroup.com).

Hector Nieto is with COMPLUTIG, 28801 Alcalá de Henares, Spain (e-mail: hector.nieto@complutig.com).

Juan Manuel Sánchez is with the Department of Applied Physics, Regional Development Institute, University of Castilla-La Mancha, 02071 Albacete, Spain (e-mail: juanmanuel.sanchez@uclm.es).

Ramón López-Urrea is with the Instituto Técnico Agronómico Provincial (ITAP), 02007 Albacete, Spain (e-mail: rlu.itap@dipualba.es).

Dalenda Mahjoub Boujnah is with the Olive Tree Institute, 40601 Sousse, Tunisia (e-mail: dalenda_boujnah@yahoo.fr).

Gilles Boulet is with the Center for the Study of the Biosphere from Space, National Centre for Scientific Research (CNRS), National Centre for Space Studies (CNES), Research Institute for Development (IRD), Paul Sabatier University (UPS), and the National Research Institute for Agriculture, Food and Environment (INRAE), Université de Toulouse, 31401 Toulouse, France (e-mail: gilles.boulet@ird.fr).

Digital Object Identifier 10.1109/JSTARS.2021.3122573

I. Introduction

THE SUSTAINABLE development goals (SDGs) form a blueprint for achieving the 2030 Agenda for Sustainable Development adopted by the United Nations in 2015. Each SDG contains numerous targets and indicators, through which the progress toward the fulfillment of the agenda can be tracked and assessed. Traditionally, this was performed by national statistical offices through classical means of data collection. More recently, analysis based on Earth observation (EO) data has been highlighted as a suitable methodology for monitoring the progress of selected targets and indicators, with overview reports and guidelines produced by the Committee on Earth Observation Satellites [1], the Group on Earth Observation [2] and the European Space Agency [3], among others. By utilizing EO data in the assessment of the SDG progress, consistency across political and natural boundaries can be established, resulting in an increase of transparency and trust in the process.

The SDG target 6.4, which focuses on the increase of the water-use efficiency and ensuring sustainable withdrawals and supply of freshwater, has been consistently selected as being able to benefit from EO data. This target consists of two indicators, 6.4.1 "Change in water-use efficiency over time" and 6.4.2 "Level of water stress: Freshwater withdrawal as a proportion of available freshwater resources." Both the indicators are concerned with water use across all sectors on economy, from energy production and industry through domestic consumption to agriculture [4], [5]. It is, however, the agricultural component, and in particular, the water used for crop irrigation, which is responsible for by far the largest freshwater consumption. It is estimated that worldwide this component accounts for around 70% of freshwater withdrawals with this percentage often being higher in semiarid regions with well-developed agriculture, such as the Mediterranean region [6]. Evapotranspiration (ET), mainly

consisting of soil evaporation (E) and plant transpiration (T), is the process through which water is transferred from the land surface to the atmosphere. Therefore, by quantifying ET using EO data, it is possible to account for water used in irrigation, and hence, a major component of SDG indicators 6.4.1 and 6.4.2.

As the custodian agency of the SDG target 6.4, the Food and Agriculture Organization of the United Nations (FAO) is responsible for providing guidance and tools for tracking indicators 6.4.1 and 6.4.2. To support the integration of EO data into this process, the FAO is running a web-portal called WaPOR (Water Productivity through Open access of Remotely sensed derived data[1]) that provides access to EO-based data layers required for agricultural water use monitoring. Among those layers are dekadal (10-days) maps of ET (also split into evaporation and transpiration) produced at three spatial levels: continental covering the whole of Africa and Middle East with a spatial resolution of 250 m, national with a spatial resolution of 100 m and coverage of selected countries, and subnational with a resolution of 30 m and coverage of selected agricultural areas. Different satellite input data are used at the different resolutions with continental scale relying mostly on Terra and Aqua MODIS, national scale using observations from MODIS and PROBA-V satellites and subnational scale mostly using data acquired by Landsat-7 and -8 satellites [7].

At the same time, new methods are being developed to derive actual and potential ET at high-resolution (20 m) using data coming mainly from the European Commission's Copernicus program, namely shortwave optical observations from Sentinel-2 (S2) satellites, thermal observations from Sentinel-3 (S3) satellites, and meteorological data from the Copernicus Climate Data Store (CDS) [8], [9]. Through the fusion of data originating from these three sources, it should be possible to obtain consistent ET estimates at the three WaPOR spatial scales. The advantages of utilizing the Copernicus data are their high data quality as well as long-term continuity and evolution plans, allowing for the establishment of solid baseline and reliable progress monitoring through 2030 and beyond. This is especially relevant to indicators such as 6.4.1, which explicitly focus on change over time.

The aim of this study is to demonstrate the suitability of Copernicus data for operational production of ET, which fulfills the WaPOR criteria, i.e., country-wide, accurate, and consistent estimation of ET at different spatial resolutions, ranging from 20 to 300 m. For this purpose, three ET datasets are validated and compared: WaPOR ET product (see Section II-A) downloaded from the WaPOR portal; ET derived with ETLook model [10] (see Section II-B) driven by Copernicus inputs (see Sections III-A–III-C), and hereafter, called ETLook$_C$; and ET derived by the TSEB-PT model [11] (see Section III-E) driven by Copernicus inputs (TSEB-PT$_C$). Ground validation was performed against *in situ* Eddy Covariance (EC) towers and large precision weighing lysimeters in agricultural areas in Tunisia and southeastern Spain (see Sections IV and V-A), while intercomparison between datasets was performed over the whole of Tunsia and Bekaa valley in Lebanon (see Sections V-B and V-C). This is followed by a discussion on the suitability of Copernicus data for ET modeling, features, and limitations of the proposed approach and comparison with WaPOR ET (see Section VI). Dekadal TSEB-PT$_C$ and ETLook$_C$ maps at the three spatial levels and covering whole of Tunisia and Lebanon can be viewed online[2].

[1][Online]. Available: https://wapor.apps.fao.org

II. WaPOR Data and Methods

A. WaPOR Data

WaPOR portal provides ET maps at three different resolutions: continental scale at 250-m resolution (called Level 1), national scale at 100-m resolution (called Level 2), and subnational scale at 30-m resolution (called Level 3). The maps represent dekadal (10-day) composites of ET, which contain the average daily ET during the compositing period. While meteorological input forcing at the three levels is the same (GEOS-5 with 0.25 ° spatial and hourly temporal resolutions for air temperature, humidity, and wind speed and MSG with 0.05° spatial and 15-min temporal resolutions for solar irradiance), the satellite data differ. For Level 1, both shortwave-optical and thermal data are obtained from MODIS sensor on board Terra and Aqua satellites. At Level-2, thermal data are still acquired by MODIS but shortwave-optical comes from PROBA-V observations (Sentinel-2 since 2020). For Level-3 modeling, both types of data come from Landsat satellites. The different data sources are summarized in Table I, which reproduce tables from Section 3 of "WaPOR Data Manual, Evapotranspiration v2.2"[3] [7]. The geographical coverage of the WaPOR portal is currently the whole of Africa and Middle-East, and therefore, no data are available for southeastern Spain.

B. ETLook ET Model

ETLook model [10] is used in the WaPOR portal and the model equations are described in detail in Section 5 of "WaPOR Data Manual, Evapotranspiration v2.2" [7]. ETLook considers soil evaporation and vegetation transpiration as two separate fluxes. It ensures energy balance at the land surface but does not estimate latent heat flux as a residual of the other energy fluxes. Instead it assumes that both E and T are transferring water into the atmosphere at rates based on the Penman–Monteith equation [12] and modulated using a number of stress factors

$$E = \frac{\Delta(R_{n,\text{soil}} - G) + \rho c_p \frac{\Delta_e}{r_{a,\text{soil}}}}{\Delta + \gamma\left(1 + \frac{r_{\text{soil}}}{r_{a,\text{soil}}}\right)} \tag{1a}$$

$$T = \frac{\Delta(R_{n,\text{canopy}}) + \rho c_p \frac{\Delta_e}{r_{a,\text{canopy}}}}{\Delta + \gamma\left(1 + \frac{r_{\text{canopy}}}{r_{a,\text{canopy}}}\right)} \tag{1b}$$

where Δ (mbar K^{-1}) is the slope of the saturation vapor pressure curve, Δ_e (mbar) is the vapor pressure deficit, ρ (kg·m^{-3}) is

[2][Online]. Available: https://et4fao.dhigroup.com/ (last accessed: Jun. 11, 2021)

[3][Online]. Available: https://bitbucket.org/cioapps/wapor-et-look/downloads/FRAME_ET_v2_data_manual_finaldraft_v2.2.pdf

TABLE I
WAPOR INPUT DATA SOURCES USED FOR THE PRODUCTION OF 2019 EVAPOTRANSPIRATION DATA COMPONENTS (E AND T) AT LEVELS 1, 2, AND 3, WHICH ARE AVAILABLE FOR DOWNLOAD FROM WAPOR PORTAL. EXTRACTED FROM [7]

Input data component	Type of inputs	Sensor	Data Product	Level 1	Level 2	Level 3
Weather data (temperature, specific humidity, wind speed, air pressure, aerosol optical depth)	Model		GEOS-5	X	X	X
Atmospheric transmissivity	Model	MSG		X	X	X
Elevation, slope and aspect	Static		SRTM	X	X	X
Land cover	Static		Copernicus Global Land Cover 2019	X	X	X
Surface albedo	Sensor	MODIS	MOD09GA, MOD09GQ	X		
		Proba-V			X	
		Landsat 7 ETM+, Landsat 8 OLI	L1TP			X
NDVI	Sensor	MODIS	MOD09GQ	X		
		Proba-V			X	
		Landsat 7 ETM+, Landsat 8 OLI	L1TP			X
Land surface temperature	Sensor	MODIS	MOD11A1, MYD11A1	X	X	
		Landsat 7 ETM+, Landsat 8 TIRS	L1TP			X

the air density, c_p (J·kg^{-1}·K^{-1}) is specific heat of dry air, γ (mbar K^{-1}) is the psychometric constant, $R_{n,\text{soil}}$ and $R_{n,\text{canopy}}$ are the net radiations at soil and canopy, respectively, $r_{a,\text{soil}}$ and $r_{a,\text{canopy}}$ are aerodynamic resistances for soil and canopy, respectively, and r_{soil} and r_{canopy} are resistances of soil and canopy respectively. All resistances are in s·m^{-1}.

The stress factors are included in the equations for resistances of soil and canopy

$$r_{\text{soil}} = b(S_e^{\text{top}})^c \tag{2a}$$

$$r_{\text{canopy}} = \left(\frac{r_{s,\min}}{\text{LAI}_{\text{eff}}}\right)\left(\frac{1}{S_t S_v S_r S_m}\right) \tag{2b}$$

where b and c are soil resistance parameters, $r_{s,\min}$ (s·m^{-1}) is the minimum stomatal resistance, and LAI_{eff} is the effective leaf area index (LAI). For *E*, the only stress factor is based on the top-soil moisture (S_e^{top}), while *T* is impacted by air temperature stress (S_t), vapor pressure stress (S_v), radiation stress (S_r), and root-zone soil moisture stress (S_m) [13].

As described previously, ETLook requires soil moisture to estimate ET. However, soil moisture is not included in either WaPOR or Copernicus inputs. Instead it is estimated based on land surface temperature (LST) and vegetation fractional cover (f_C). Following the method of Yang *et al.* [14], a trapezoid is constructed in the LST-f_C space with corner values estimated based on theoretical considerations. The soil moisture of a given pixel is then estimated based on the relative location of LST and f_C within the theoretical trapezoid by inverting the Penman–Monteith equation for both dry and moist bare soil and vegetation conditions.

III. COPERNICUS-BASED DATA AND METHODS

Three sets of Copernicus data are used to produce both ETLook$_C$ and TSEB-PT$_C$ datasets: meteorological, Sentinel (Earth observation) and ancillary. In order to compare against the WaPOR dataset, ET is also produced at three spatial resolutions comparable to WaPOR Level 1, Level 2, and Level 3 data.

TABLE II
SPATIAL RESOLUTIONS AND MAIN SATELLITE DATA SOURCES USED AT THOSE RESOLUTIONS FOR THE THREE SPATIAL LEVELS OF WAPOR, ETLOOK$_C$, AND TSEB-PT$_C$ ET DATASETS

Spatial Level	WaPOR ET res.	WaPOR Sensors	ETLook$_C$ and TSEB-PT$_C$ ET res.	ETLook$_C$ and TSEB-PT$_C$ Sensors
Level 1	250 m	MODIS on Terra and Aqua	300 m	SLSTR and OLCI on Sentinel-3A/B
Level 2	100 m	MODIS on Terra and Aqua and Vegetation on PROBA-V	100m	SLSTR on Sentinel-3 A/B and MSI on Sentinel-2 A/B
Level 3	30 m	OLI/TIRS on Landsat 8 and ETM+ on Landsat 7	20 m	SLSTR on Sentinel-3 A/B and MSI on Sentinel-2 A/B

However those resolutions differ slightly due to spatial characteristics of the satellite sensors used, as shown in Table II. The preprocessing and ET modeling methods used with Copernicus data are described in the subsequent sections.

A. Copernicus Meteorological Data

Meteorological inputs, which are critical for accurate estimation of ET, are based on ERA5 reanalysis dataset [15] produced by the European Center for Medium Range Weather Forecasts and distributed freely and openly through the Copernicus CDS.[4] The ERA5 data contain surface meteorological parameters covering the whole Earth on 30-km grid and hourly temporal resolution and going back to 1950.

Both instantaneous and daily forcing were derived from ERA5 data. Instantaneous weather at the satellite overpass are used to drive the ET models and include air temperature, vapor pressure, wind speed, surface pressure, and clear-sky solar irradiance. All instantaneous data were obtained by linear interpolation between two ERA5 hourly time slots to the time of Sentinel-3 SLSTR

[4][Online]. Available: cds.climate.copernicus.eu

acquisition over the area of interest. Daily parameters are used to extrapolate and interpolate the instantaneous estimates of ET and include solar irradiance as well as air and dew temperatures, wind speed, and pressure, which are then used to calculate the reference ET. They were integrated over a 24-h period starting at midnight local time. A digital elevation model (DEM) with a resolution of 300 m (see Section III-C) was used to enhance the spatial resolution of the meteorological inputs as described below.

Instantaneous air temperature was based on 2-m air temperature ERA5 variable. Due to the low spatial resolution of the meteorological data, it was assumed that the air temperature that better represents meteorological conditions at that resolution is the temperature at atmospheric blending height (set to be 100 m above ground), where the impact of local surface conditions on those parameters is not so direct. The resolution of air temperature was additionally enhanced by using a 300-m resolution DEM (see Section III-C) and standard lapse rate of 6.5 K/1000 m [16] to correct for temperature variations due to changes in elevation between 2 m above the geopotential height at which ERA5 temperature was produced and the 100-m above DEM surface elevation.

Vapor pressure was derived from 2 m dew point temperature ERA5 field. Similarly to air temperature, it was assumed to represent conditions at blending height and was corrected for changes in elevation using DEM and moist air lapse rate of 2 K/1000 m [16].

Wind speed was based on 100 m "u" and "v" ERA5 wind components. Apart from trigonometric calculation to obtain total magnitude of wind speed no other preprocessing was performed.

Surface pressure is based on ERA5 field of the same name. Similarly to air temperature, it was corrected for changes due to varying elevation using a DEM.

The final instantaneous parameter was surface solar irradiance. Clear sky conditions were assumed since this parameter is only used at a time and place where thermal observations of the surface by the Sentinel-3 satellite were possible. In addition, solar irradiance was also corrected by elevation, incidence angle, and terrain shading. First, clear-sky irradiance on a horizontal surface was estimated using aerosol optical thickness at 550 nm, total column water vapor, and air temperature ERA5 fields [17]. Subsequently this was corrected for elevation and terrain orientation to estimate irradiance on a tilted surface [18].

Daily solar irradiance is calculated using 24-h integration of ERA5 downward surface irradiance product and clear sky irradiance estimated as described previously. At each hourly timestep, a cloudiness factor is first estimated using the ratio of surface to horizontal clear sky irradiance. Based on this, beam and diffuse radiation components are derived and corrected for terrain orientation similarly as was done with the instantaneous clear-sky irradiance, and finally, integrated to daily values.

Finally, the reference ET is estimated using the FAO56 model [19]. It is calculated using daily mean values of air temperature, dew point temperature, wind speed, surface pressure, and surface solar radiation products. All the relevant terrain corrections are applied to those products before they are used in the FAO56 model.

B. Copernicus Sentinel Data

Data acquired by MSI sensor on S2 satellites and SLSTR and OLCI sensors on S3 satellites are essential ET model inputs. This section outlines the characteristics of these data and basic preprocessing steps, while in Section III-D, the details of the methods used to derive biophysical inputs to the ET models at different spatial levels are presented.

MSI on Sentinel-2 A and Sentinel-2B satellites provides high-resolution multispectral shortwave observations of Earth's surface with a geometric revisit time at the equator of 5 days [20]. Of particular relevance for characterizing surface biophysical properties are four bands in the visible and near-infrared spectrum, and three bands in the red-edge and two bands in the shortwave-infrared region. Those bands were downloaded as L1C S2 product and used as input to Sen2Cor atmospheric correction model to obtain 20-m top-of-canopy (TOC) reflectance [21]. Cloud and shadow masking was done based on the output of the Fmask [22] cloud masking model, instead of the quality layer of Sen2Cor output, due to inaccuracies present in Sen2Cor cloud mask. The cloud-masked TOC bands are used to produce biophysical inputs to the ET model at 20-m spatial resolution. In addition, they are used to sharpen the SLSTR LST, which is also needed to model ET at 20-m resolution.

Sentinel-3 A and Sentinel-3B satellites carry multiple EO sensors, including the multispectral OLCI with a spatial resolution of 300 m, and SLSTR that acquires shortwave optical observations at 500-m resolution and thermal-infrared observations with 1-km resolution [23]. Part of the shortwave bands of OLCI and SLSTR overlap with those of MSI, and therefore, are also highly suitable for the land surface biophysical characterization, while the thermal bands of SLSTR are used to obtain LST. The two-satellite S3 constellation has a daily geometric revisit frequency at the equator, meaning that potentially ET can be estimated daily (ignoring cloudiness). Sentinel-3 Synergy SY_2_SYN product, which combines the surface reflectance from shortwave optical bands on OLCI and SLSTR instruments, was used to characterize surface biophysical properties at 300-m spatial resolution and to sharpen SLSTR LST to 300 m. S3 SLSTR L2 product contains LST, which is required to characterize energy fluxes at the land surface, including ET. Invalid pixels were identified using the mask_in layer of the L2 file and the following more conservative rules:

1) LST $<$273.15 K;
2) LST—air temperature <-2 K; and
3) view zenith angle $>45°$.

Minimum view zenith angle (VZA) compositing was used in case of multiple SLSTR observations of the same area on the same day (i.e., acquisitions by both Sentinel-3 A and Sentinel-3B). This was done under the assumptions that smaller VZA would result in more accurate LST retrieval due to both shorter atmospheric path and reduced thermal directional effects.

C. Ancillary Data

In order to run both ETLook and TSEB-PT models with Sentinel data, two ancillary sources of data were also used:

TABLE III
LAND-COVER-BASED LOOKUP TABLE FOR ANCILLARY PARAMETERS USED IN ET MODELS

CGLC-LC	$h_{C,min}$ (m)	$h_{C,max}$ (m)	PAI_{max} (-)	f_C (-)	w_C/h_C (-)	l_w (m)	χ	r_{st} (s/m)
20	2	2	0	1	1	0.05	1	175
30	0.1	1	4	1	1	0.02	0.5	175
40	0.15	1.5	5	1	1	0.02	0.5	125
41	0.15	1.5	5	1	1	0.02	0.5	125
42	0.15	1.5	5	1	1	0.02	0.5	125
43	0.15	1.5	5	1	1	0.02	0.5	125
50	10	10	0	0	0	0	0	400
60	0.1	0.1	0	0	0	0	0	100
70	0.1	0.1	0	0	0	0	0	100
80	0.1	0.1	0	0	0	0	0	100
81	0.1	0.1	0	0	0	0	0	100
90	2	2	5	1	1	0.1	1	150
100	0.3	0.3	0	1	1	0.005	1	180
111	10	10	0	0.8	2	0.05	1	300
112	5	5	0	0.8	1	0.15	0.7	180
113	10	10	0	0.8	2	0.05	1	300
114	8	8	0	0.8	1	0.15	0.7	190
115	8	8	0	0.8	1.5	0.1	0.8	200
116	5	5	0	0.8	1.5	0.1	0.8	180
121	5	5	0	0.3	1.5	0.05	0.8	250
122	4	4	0	0.3	1	0.15	0.7	180
123	5	5	0	0.3	1.5	0.05	0.8	250
124	4	4	0	0.3	1	0.15	0.7	200
125	5	5	0	0.3	1.5	0.1	0.8	180
126	3	3	0	0.3	1.5	0.1	0.8	250
200	0.1	0.1	0	0	0	0	0	100

CGLC-LC is the land cover code for the Copernicus Global Land Cover Legend (https://land.copernicus.eu/global/products/lc); $h_{C,\text{min}}$ is the minimum canopy height; $h_{C,\text{max}}$ is the maximum canopy height occurring when plant area index (PAI) reaches its maximum PAI_{max}; f_C is the at-Nadir fraction of the ground occupied by a clumped canopy ($f_C = 1$ for a homogeneous canopy); w_C/h_C is a canopy shape parameter, representing the canopy width to canopy height ratio; l_w is the average leaf size; χ is the campbell [24] leaf angle distribution parameter; and r_{st} is minimum stomatal resistance.

Copernicus Global Land Cover (CGLC) for year 2019 and Shuttle Radar Topography Mission (SRTM) DEM.

The CGLC map was selected as it is also used as input to current WaPOR products. Land cover map is used to assign ET model parameters, which are difficult to estimate directly from other satellite data. Those parameters, and values assigned to different land cover classes, are listed in Table III. The TSEB-PT model (see Section III-E) requires all of the parameters, apart from stomatal resistance. The ETLook model (see Section II-B) requires only maximum vegetation height and stomatal resistance and the values for those two parameters were extracted directly from the WaPOR documentation. Values of other parameters were obtained from [9].

SRTM DEM was selected because it is used as default data input in the Sen2Cor algorithm and also it is the DEM used in the WaPOR methodology. The DEM is used for three main purposes: during Sen2Cor atmospheric correction, to correct ERA5 meteorological parameters for terrain effects (elevation and illumination conditions), and in the thermal sharpening model to add elevation and illumination conditions as predictor variables.

D. Input Data Preparation While Ensuring Consistency Across Spatial Scales

As outlined in Sections III-A–III-C, the Copernicus inputs to the ET models consists of meteorological data, Sentinel data, and ancillary data. It is important to explicitly consider the requirement for consistency of modeled ET across the three spatial levels (see Table II) when preprocessing those inputs. Since the Level 2 (100 m) and Level 3 (20 m) products use exactly the same inputs, it was decided to prepare the inputs and run the ET models at 20-m resolution and only at the end to resample the output ET maps to 100 m. This means that Copernicus inputs have to be prepared for the 300 m and the 20-m ET models runs.

ET modeling at both Level 1 and Level 3 uses the same meteorological data. As explained in Section III-A, the resolution of meteorological inputs is sharpened from original 30 km to 300 m (Level 1 resolution) using a DEM. Any further enhancement beyond 300 m was achieved using bilinear interpolation. Similarly, ancillary data are the same across all spatial levels. The CGLC map has original resolution of 100 m. It was resampled using mode resampling for the 300-m models runs and using nearest-neighbor resampling for the 20 m runs. After the resampling, the parameters from Table III were applied.

The main difference between Level 1 and Level 3 inputs lies in the shortwave optical observations needed for setting surface biophysical parameters. For Level 3 inputs, the TOC S2 reflectance was used within the biophysical processor available in SNAP v8 software[5] and subsequent Python scripts to derive LAI, fraction of vegetation that is green (f_g—green LAI over total LAI), vegetation gap fraction observed at the sensor viewing angle ($f_C(\theta)$), and leaf broadband bihemispherical reflectance and

[5][Online]. Available: http://step.esa.int/main/

transmittance and soil broadband bihemispherical reflectance as described in [9, Sec. 2.3.1]. One major modification was that, in previous studies, the soil broadband reflectance was given a constant value of 0.15 in the visible (VIS) spectrum and 0.25 in the shortwave infrared (NIR). In this study, bulk surface broadband reflectance in VIS and NIR were first estimated based on TOC reflectance output by Sen2Cor and narrow- to broad-band conversion coefficients derived through 125 simulations of 6S radiative transfer model [25] covering a wide range of different atmospheric conditions. The bulk broadband reflectance was then used together with leaf broadband bihemispherical reflectance and vegetation gap fraction to derive soil broadband reflectance in both VIS and NIR. This method quickly becomes unstable as $f_C(\theta)$ increases, and therefore, was used only in pixels, which were predominantly bare (i.e., $f_C(\theta) < 0.25$), whereas those pixels with significant vegetation cover ($f_C(\theta) > 0.25$) used the aforementioned constant values of 0.15 and 0.25 for VIS and NIR, respectively, considering that vegetated areas usually have darker background surfaces due to larger soil organic matter concentration.

A simple temporal compositing scheme was used to reduce data gaps due to clouds in S2 observations. For each date on which ET was to be modeled (i.e., thermal SLSTR data were available), all S2 images falling within 10 days were selected. The cloud free pixels were iteratively picked from the selected images starting with the ones closest to the target date. This was performed for TOC reflectance and all derived biophysical parameters.

The Sentinel-3 SYN product was used to derive biophysical parameters for Level 1 model runs. Since there are no operational biophysical SYN-based LAI and pigment concentrations products, a method was developed in which a machine-learning (ML) model (random forest) was trained using an S2 biophysical parameter resampled to 300 m and S3 Synergy reflectance. The model was then applied to S3 Synergy reflectance to derive the biophysical parameters at 300-m resolution. In order to preserve observation geometry between S2 and S3 acquisitions (i.e., close to nadir view) a 10-day VZA composite was created from SY_2_SYN products before training and applying the biophysical ML model. Result of this method are biophysical products that are consistent across sensors (MSI and SYN) and spatial scales (20 and 300 m) as shown in Fig. 1. It is worth noting that this approach trains the model from any available S2 tile within the SYN footprint, and does not require processing of all S2 tiles falling within the footprint as long as the surface properties of the few S2 tiles used within the larger S3 scene are representative of the whole scene. The trained model can then be applied to the whole SYN scene without any significant loss of accuracy.

Finally, the Sentinel-3 SLSTR LST product was used as input for model runs at all spatial levels. The data mining sharpener (DMS) was used to sharpen the minimum VZA LST daily composite at a spatial resolution of around 1 km, using shortwave reflectance and DEM at higher spatial resolution as described in [9]. Temporal composite of S2 TOC reflectance with 20-m resolution and centered on the date of S3 overpass was used in case of sharpening to 20 m. When sharpening to 300 m, the SY_2_SYN product acquired at the same time as LST was used. The DMS ensures that thermal energy is conserved during the sharpening process [26], which leads to consistent LST maps at 20-m and 1-km resolutions.

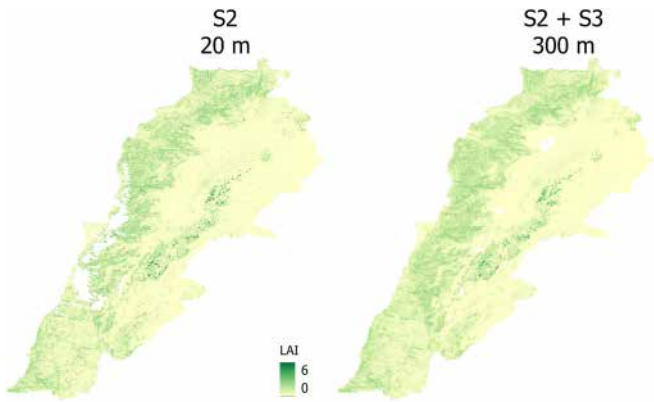

Fig. 1. Maps of S2 LAI versus S3 Synergy LAI derived using S2-S3 biophysical data fusion on 25 June 2019 in Lebanon.

E. TSEB-PT ET Model

TSEB-PT stands for two-source energy balance—Priestley Taylor [11] and it is the ET model, which was shown in [9] to produce most accurate land-surface energy fluxes compared to two other approaches when driven by Copernicus inputs. The model considers vegetation and soil as two sources of land-surface energy fluxes. The energy transfer from the sources into the atmosphere is estimated separately, although they are linked (in an analogy to electrical circuits) by resistances to heat transfer, which are arranged in a series network. The model estimates net radiation of both canopy and soil ($R_{n,C}$ and $R_{n,S}$, respectively), sensible heat flux of both canopy and soil (H_C and H_S, respectively), and ground heat flux (G). Since energy balance must hold, latent heat flux, which is the energy used for phase conversion from liquid water to vapor, of both canopy and soil (LE_C and LE_S, respectively) is calculated as the residual of the other fluxes

$$\mathrm{LE}_C = R_{n,C} - H_C \tag{3a}$$

$$\mathrm{LE}_S = R_{n,S} - H_S - G. \tag{3b}$$

Since the model has to estimate energy fluxes of both soil and canopy based on a single bulk LST measurement, it initially takes the assumption that vegetation is transpiring at a potential rate based on the Priestley–Taylor equation. This first guess transpiration is iteratively reduced within the model in case unrealistic fluxes are obtained (e.g., negative latent heat fluxes for either soil or canopy during daytime). TSEB-PT estimates instantaneous fluxes at the time of thermal image acquisition in units of $\mathrm{W{\cdot}m^{-2}}$. They are then extrapolated to daily ET (mm/day) based on the assumption that the ratio of the latent heat flux to solar irradiance remains invariant during day-time hours [27]. More details on the TSEB-PT model and the way it was applied can be found in [9, Sec. 2.1 and 2.1.2].

Fig. 2. Overview maps of (a) Tunisian olive orchard and (b) Spanish potato, grapevine, festuca, and almond, and (c) wheat field validation sites, with Sentinel-2 images from July used as background. Studied parcels are outlined in black and locations of flux towers are indicted as red dots.

F. ET Gap Filling

Both TSEB-PT and ETLook produce daily ET estimates on days with thermal data acquisitions and for pixels that are not obscured by clouds or shadows during the satellite overpass. The WaPOR portal delivers decadal (10-day) composites of ET, which contain the average daily value of ET during the compositing period. If the average was derived only from estimates obtained during sunny conditions, then this would lead to an overestimation of dekadal ET. Therefore, it is important to gap fill the time series and to take the conditions present during cloudy periods into account.

For outputs of both models driven by Copernicus data, the gaps in the daily ET maps due to cloudy conditions were filled using maps from adjacent dates (with up to 10-day temporal displacement) and an assumption that the ratio of reference to actual ET (i.e., the product of FAO56 crop and water stress coefficients [19]) remains steady over short periods. Since reference ET depends only on meteorological parameters, it is possible to estimate it also during cloudy periods. This approach takes the changing meteorological conditions during the cloudy periods (e.g., reduced solar irradiance and reduced air temperature) into account. At the same time, fine spatial details are retained since actual ET from adjacent dates, estimated at a higher spatial resolution than reference ET, is also used during gap filling.

A recent study that evaluated a number of ET gap-filling reference quantities has shown that using reference ET tends to underestimate gap-filled actual ET during long gap periods (8 days or more), since water stress is usually smaller in cloudy conditions [28]. However, when looking at shorter gap periods (1–3 days), reference ET performed as well as other, even more complex, reference quantities. Since in this study, we are gap filling between cloud-free Sentinel-3 LST observations, which are acquired daily, a very large majority of gaps will be short. Therefore, we expect the chosen method to perform well in this study.

IV. Field Validation Data

The focus of this assessment is on numerical and statistical analysis, trying to avoid applying expert knowledge criteria. *In situ* observations from EC towers and large weighing lysimeters, despite not being free of uncertainties, are, therefore, considered our "ground-truth." Note that at all the EC sites, the energy closure correction of measured data was performed by assigning the residual part to latent heat flux [29], with exception of the wheat site (see Section IV-B), where a higher closure is expected due to the large field extension, and corrections may introduce some artifacts. However, we also show time-series figures with the agreement for all possible range of dekadal ET due to the EC energy imbalance closure.

The validation is performed at six field measurements sites: a rainfed olive grove in Tunisia and five other sites, either in irrigated or rainfed, located near Albacete, Spain (see Fig. 2). Even though Lebanon is one of the main regions of interest of this study, technical and economic issues prevented access to *in situ* validation data for the study period. The sites located in southeast Spain, with a similar climate to that of Tunisia and Lebanon, and containing various crops and irrigation systems, have therefore, been included to ensure a more robust model validation despite lack of WaPOR ET in that area.

A. Tunisia

A rainfed olive orchard provided with an EC tower and located at the Olive Tree Institute research station of Taoues (10.60153° E, 34.93111° N), about 40 km far from Sfax, was used as the validation site in Tunisia. The tower setup is as described in [30] although the location is slightly changed. Trees are planted 24-m apart (17 trees/ha), with a very low tree canopy cover fraction ranging from 5% to 10%. A 10-m tower was installed over a tree and a 3-m tower over the bare soil, the net radiation and soil heat flux components being thus computed as the area average values. Data have been provided by CESBIO (France) and the Olive Institute (Tunisia), and consists of 30-min flux data (net radiation and ground, sensible, and latent heat fluxes). Additional postprocessing of the EC data has consisted of detecting and removing outliers for the half-hourly EC flux time series [31], followed by a gap filling based on evaporative fraction.

B. Southeast Spain

These sites are located in the province of Albacete (Spain) and are managed by the University of Castilla-La Mancha (UCLM) and the Technical Institute of Agronomy of Albacete Province (ITAP). Most of the sites are located in Las Tiesas Experimental Farm near Barrax, which has been used as a long-term site

TABLE IV
DESCRIPTIVE AND ERROR METRICS BETWEEN ESTIMATED DEKADAL ET (MM/DAY) AND *IN SITU* DEKADAL ET (MM/DAY)

site	N	$\overline{Obs.}$	model	$\overline{bias}$	MAE	RMSE	fMSE_u	fMSE_s	a	scale	r	d
All	137	3.04	TSEB-PT	0.29	0.75	0.96	0.56	0.44	0.67	1.35	0.90	0.92
			ETLook	1.39	1.44	1.69	0.89	0.11	0.60	1.51	0.91	0.78
olive	26	1.08	TSEB-PT	0.09	0.43	0.59	0.25	0.75	0.58	1.04	0.60	0.75
			ETLook	0.46	0.72	0.95	0.88	0.12	-0.13	1.98	-0.26	0.30
festuca	33	5.33	TSEB-PT	1.05	1.14	1.38	0.81	0.19	0.55	1.47	0.81	0.75
			ETLook	2.22	2.22	2.30	0.97	0.03	0.67	1.40	0.94	0.62
potato	14	4.69	TSEB-PT	0.54	0.82	0.99	0.46	0.54	0.79	1.14	0.91	0.92
			ETLook	1.79	1.79	2.00	0.85	0.15	0.78	1.14	0.89	0.76
grapevine	20	2.05	TSEB-PT	-0.42	0.64	0.82	0.73	0.27	0.20	1.58	0.32	0.53
			ETLook	0.92	0.94	1.12	0.93	0.07	0.21	2.13	0.45	0.53
almond	24	2.60	TSEB-PT	0.31	0.68	0.75	0.82	0.18	0.17	2.15	0.36	0.53
			ETLook	1.34	1.34	1.44	0.97	0.03	0.33	2.17	0.71	0.50
wheat	20	2.20	TSEB-PT	-0.21	0.64	0.84	0.70	0.30	0.49	1.67	0.81	0.84
			ETLook	1.45	1.49	1.73	0.93	0.07	0.37	1.97	0.72	0.57

N is the number of dekads used in the validation; $\overline{Obs.}$ (mm/day) represent the average ET of *in situ* datasets; $\overline{bias}$ (mm/day) is the average bias, computed as the mean difference between the observed and the predicted; MAE is the mean absolute error (mm/day); RMSE (mm/day) is the root mean square error, which is decomposed between its unsystematic (fMSE_u) and systematic (fMSE_s) fractions (fMSE_u + $\text{fMSE}_s = 1$); *a* is the slope of the regression between the observed and the predicted; scale is the ratio between the standard deviation of the observed over the predicted;, *R* is the Person correlation coefficient between observations and predictions; and *D* is the Wilmott's index of agreement [37].

for calibration/validation operations of multiple satellite sensors and products.

A weighing lysimeter of 6.21 m^2 is installed in a field with rotating crops (2.10130° W, 39.06081° N), planted with potato in 2018 (irrigated potato site). ET at 15-min timesteps, from May to October, was calculated from weight differences before and after the period, and then, aggregated at hourly timesteps. These records were visually and manually checked for consistence, in particular, during rainfall and irrigation events, outliers flagged out, and then, gap filled based on either reference ET or net radiation flux ratio. More information on this lysimeter can be found in [32].

An irrigated grass site is adjacent to the potato field and aims to represent a reference grass layer, mainly composed of perennial *Festuca* species. An analogous weighting lysimeter of 6.21-m^2 area is placed in this site (2.10009° W, 39.06046° N). In order to keep the surface the closest to the reference conditions described by the FAO56 document (which has recently been updated [33]), this site is frequently sprinkler irrigated and clipped to a height of ca. 0.12 m. Processing of lysimeter measurements was the same as at the irrigated potato site. Data were processed and available between May and October 2018 and 2019. More information on this lysimeter and the management of this site can be found in [34].

A third lysimeter (monolithic) located at coordinates 2.10104° W, 39.05972° N is installed under a 4-ha vineyard *cv. Tempranillo* with drip irrigation. This lysimeter occupies a surface of 9 m^2 containing two grapevines. Data from May to October 2018 and from May to 15 June 2019 were available. More information on this lysimeter and the vineyard characteristics can be found in [35].

In a close by parcel (2.08965° W, 39.04228° N), an Eddy Covariance tower was deployed in a young drip-irrigated almond orchard [36]. Flux data have been fully processed and provided as daily ET estimates, from May to October 2018 and July–September 2019, both with uncorrected energy closure and corrected closure through the residual technique.

Finally, a rainfed wheat field located in the Oran farm, a few kilometers southeastern Albacete (1.85970° W, 38.82337° N) is also provided with an EC tower.[6] Data from this site were available for this study. Flux data have been fully processed and provided as daily ET estimates, from January to July 2018, covering the wheat growing season until harvesting. Direct EC measurements (noncorrected) were used in this case to prevent artifacts introduced by the net radiation component during the closure correction. The vast extension and homogeneity of this wheat plot guaranties feasible measurements of the turbulent fluxes.

V. RESULTS

A. Field-Site Validation

Error and agreement metrics between the observed and modeled values are shown in Table IV and scatter plots of modeled versus observed values are shown in Fig. 3. This table also shows the number of validation dekads used for each site as well as their mean measured ET. Both TSET-PT_C and ETLook_C models use the same remote sensing inputs, namely sharpened Sentinel-3 LST, Sentinel-2-based LAI, surface albedo, and other biophysical parameters, as well as same meteorological forcing from ERA5 reanalysis and ancillary data derived from the CGLC land cover map. Since both models are processed using 20-m Copernicus dataset, validation is done at local scale (Level 3 in the WaPOR nomenclature). A buffer of 3×3 pixels around each lysimeter was extracted as representative of the lysimeter readings, considering possible geolocation uncertainties. On the other hand, a larger buffer of 5×5 pixels, accounting for the

[6][Online]. Available: http://www.europe-fluxdata.eu/home/site-details?id=ES-FcO, last accessed: 18.06.2021

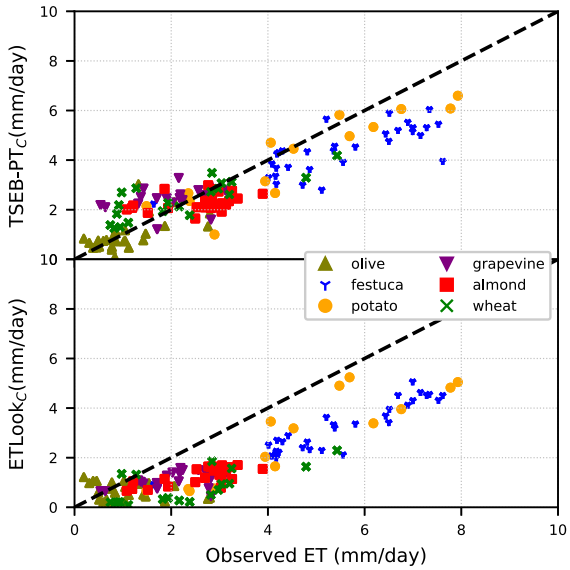

Fig. 3. Scatterplot between the *in situ* dekadal ET and estimated dekadal ET for all sites. TSEB-PT$_C$ on the top panel and ETLook$_C$ on the bottom.

typical EC flux footprint is extracted for the olive, almond, and wheat sites. It is worth noting that these statistics include the energy balance closure correction [29], with exception of the wheat field. However, Fig. 4 shows the time series with the agreement for all possible EC residual corrections.

Both models are able to track the spatiotemporal ET variability in a similar way, with correlation coefficients between the observed and predicted of 0.90 and 0.91 for TSEB-PT$_C$ and ETLook$_C$, respectively. However ETLook$_C$ shows significant larger error metrics, with a systematic underestimation showed by a mean bias on dekadal ET higher than 1.0 mm/day, whereas TSEB-PT$_C$ showed smaller bias of 0.3 mm/day. This also results in a lower RMSE in TSEB-PT$_C$ as compared to ETLook$_C$ (1.0 versus 1.7 mm/day, respectively). Willmott's Index of Agreement (*d*) [37] tries to summarize in a single value the agreement and error metrics, and as such, due to the larger RMSE and bias of ETLook$_C$, TSEB-PT$_C$ shows consistently better values of *d*, both for all individual sites and when all sites are pooled together. This can also be observed in the scatterplot between the observed and predicted (see Fig. 3), in which the predicted values for TSEB-PT$_C$ are closer to the 1:1 line.

When looking at the sites individually, ETLook$_C$ consistently shows larger systematic underestimation and standard errors than TSEB-PT$_C$. However, ETLook$_C$ also demonstrates a better capability to track temporal changes of ET (with a larger correlation coefficient than TSEB-PT$_C$) for the almond, grapevine, and festuca sites. It is known from previous studies that TSEB-PT$_C$ is quite sensitive to a correct determination of canopy structure/roughness [38]. In particular, CGLC product flags both almond and grapevine sites as croplands, which, based on the lookup table (see Table III), assigns a maximum canopy height of 1.5 m when LAI is at 5. Therefore, the canopy height is strongly underestimated in these two sites yielding larger uncertainties in TSEB-PT$_C$. ETLook$_C$ on the other hand, even though uses the same canopy height/roughness input, seems to overcome this limitation, as it computes ET from the relative position of actual LST within theoretical wet and cold boundaries. The ability of modeled ET to track temporal changes from the *in situ* measurement is shown in Fig. 4. In this figure, and for the sites with EC towers, an uncertainty band around the observed dekadal ET is displayed, due to energy imbalance closure.

The Tunisian olive site falls within the area mapped by WaPOR, with Tunisia being covered by L1 and L2 ET products. Fig. 5 shows the validation at this site of both Copernicus-based L2 ET products as well as WaPOR L2 product. WaPOR ET produces the largest bias at this site but has higher Wilmott's Index of Agreement compared to ETLook$_C$ due to improved correlation. Nevertheless, TSEB-PT$_C$ ET outperforms the two other datasets according to all statistical measures.

B. Cumulative Monthly and Annual Maps

In addition to point-scale validation against field measurements, a spatiotemporal intercomparison was performed between models and data sources. For that purpose, we will focus on the two regional study areas, Lebanon and Tunisia, for which ET data are available in the WaPOR portal. For Lebanon, the three processing levels are available, as WaPOR portal provides Level 3 data for the Bekaa Valley, an area with an intensive irrigation perimeter, whereas for Tunisia, only Level 1 and Level 2 ET are available. In this section, we will use the level with highest spatial resolution for each region. Results presented in this and subsequent section are based on ET data covering the whole year 2019.

The differences between TSEB-PT$_C$, ETLook$_C$ and WaPOR Level 2 ET in Tunisia are summarized in annual cumulative maps of Fig. 6, with Fig. 7 showing the monthly evolution of the ET for the three datasets. Monthly maps show a higher spatial variability within TSEB-PT$_C$ dataset, with northern areas showing overall larger ET rates in all months. It also shows some regional features with higher rates in April and September, as compared to ETLook$_C$, which could be caused by rainfall events. Fig. 6 also shows the absolute difference between models in terms of annual cummulative ET, as well as the ratio of the intra-annual dekadal standard deviation between models. The annual maps make it clear that the differences between models show a S-N gradient. Regarding models produced with Copernicus data, ET rates show larger values in TSEB-PT$_C$ than ETLook$_C$ in the North, with also a higher temporal variability ($\sigma_{\text{TSEB}-\text{PT}_C}/\sigma_{\text{ETLook}_C} > 1$), while in the South, ETLook$_C$ yields higher ET annual rates and higher temporal variability ($\sigma_{\text{TSEB}-\text{PT}_C}/\sigma_{\text{ETLook}_C} < 1$). While comparing WaPOR product with Copernicus-based models, the former tends to provide overall lower ET rates, most notably in the northern areas and against TSEB-PT$_C$, and lower temporal variability, mostly in the southern areas. To finalize, it is worth remarking that some gaps exists when comparing standard deviations in large areas in southwest Tunisia. This is caused by the fact that WaPOR seems to constantly provide zero dekadal ET rates for all timesteps, resulting, therefore, in null annual standard deviation (i.e., $\sigma_{\text{WaPOR}} = 0$), and hence, arithmetic indeterminate form when computing its ratio between models ($\sigma_j/\sigma_{\text{WaPOR}}$).

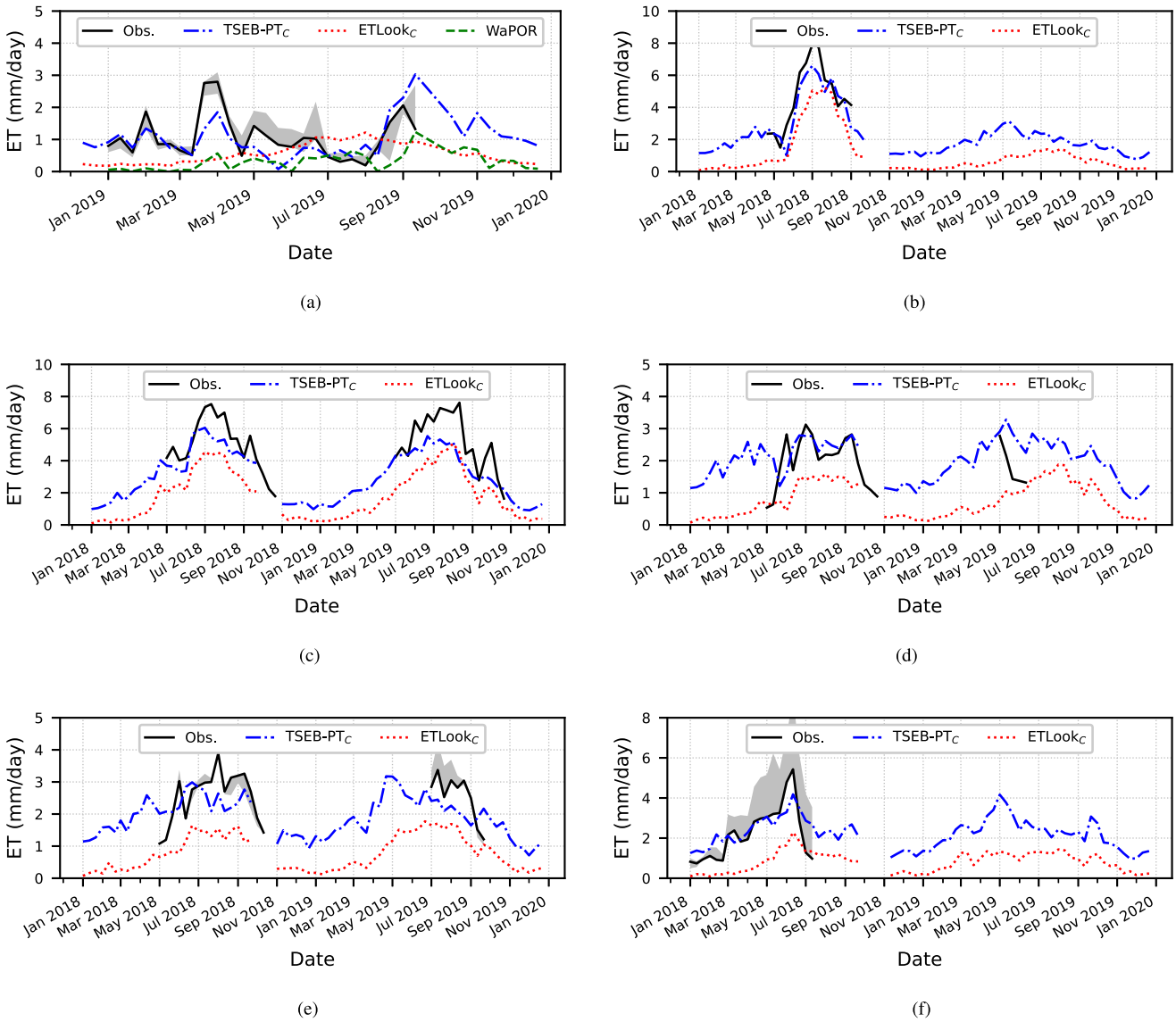

Fig. 4. Dekadal time series of measured and modeled ET at all the validation sites. At the EC sites [4(a), 4(e), and 4(f)], the grayed area shows the uncertainty band around measurements due to the surface energy imbalance, which is computed as the range values between the uncorrected ET, ET corrected by Bowen Ratio, and ET corrected by the residual method. (a) Olive. (b) Potato. (c) Festuca. (d) Grapevine. (e) Almond. (f) Wheat.

The model intercomparison in Lebanon is performed using Level 3 (20/30 m) over the Bekaa Valley, as it is the area of interest with availability of WaPOR Level 3 ET. Similarly to Tunisian comparison, Fig. 8 illustrates annual cumulative ET maps and model intercomparison for this region, while Fig. 9 shows the cumulative monthly maps for the three datasets. Since Level 3 for WaPOR and Copernicus are provided at different resolutions (30 and 20 m, respectively), the per-pixel intercomparison maps depicted in Fig. 8 were produced by resampling WaPOR L3 data, both annual cummulative ET and intra-annual dekadal standard deviation, to 20 m using bilinear interpolation.

In this case, the monthly maps show similar spatiotemporal patterns in all products, with irrigated areas showing larger ET rates during summer months than the rainfed and natural vegetation surfaces. Nevertheless, ETLook models tend to yield lower ET rates in nonirrigated areas in summer and all areas in winter compared to TSEB-PT$_C$.

Considering the annual analysis, similarly to observations in Tunisia, TSEB-PT$_C$ tends to produce higher ET rates than ETLook runs. In addition, WaPOR shows a larger temporal variability than TSEB-PT$_C$ ($\sigma_{\text{TSEB}-\text{PT}_C}/\sigma_{\text{WaPOR}} < 1$) within irrigation perimeters, whereas the opposite is observed in rainfed areas.

C. Robustness Across Scales

Considering that mass and energy must be preserved between scales, this analysis evaluates the robustness of the models/data sources to produce sound estimates across all available levels. In the first step, the dekadal ET (in mm/day) was resampled using averaging, from a higher level to a lower one. With the resampled product at the lower resolution, annual cumulative ET and intraannual dekadal standard deviation of both levels (i.e., resampled high-resolution and original coarse-resolution levels) were compared.

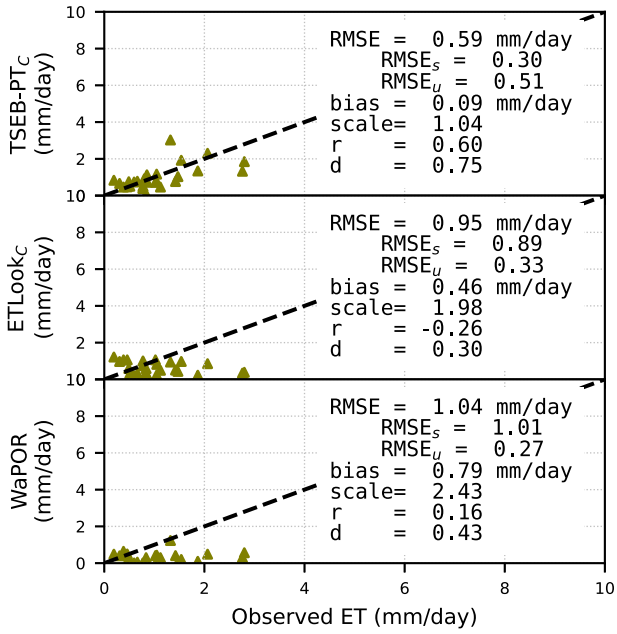

Fig. 5. Scatterplot between the *in situ* dekadal ET and estimated TSEB-PT$_C$, ETLook$_C$, and WaPOR ET at the Tunisian olive grove EC tower.

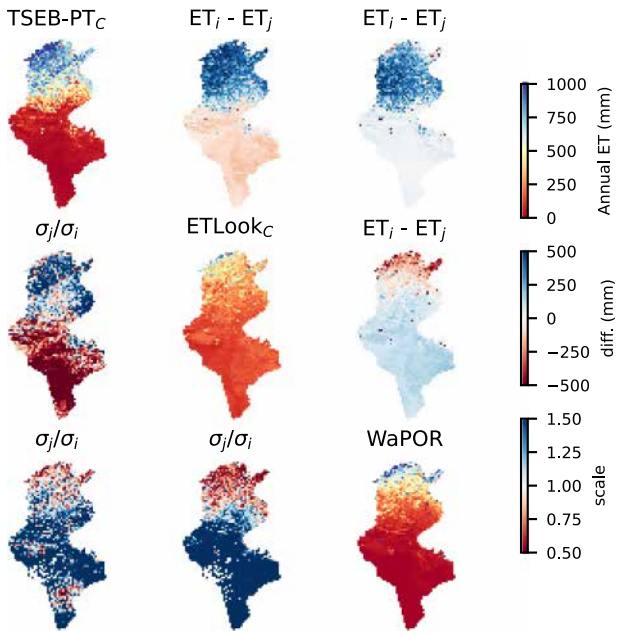

Fig. 6. Annual comparison of TSEB-PT$_C$, ETLook$_C$, and WaPOR Level 2 (100 m) ET output in Tunisia for year 2019. Maps in the diagonal show each model cumulative annual ET. The off-diagonal represents model intercomparisons, both in ET differences (upper right) and in intra-annual dekadal standard deviations scale (lower left). "*i*" in the model comparison grid represents the model in row and "*j*" is the model in the column.

Fig. 10 shows the differences between Levels 1 and 2 for the three ET products (TSEB-PT$_C$, ETLook$_C$, and WaPOR) in both Tunisia and Lebanon. Particularly in Lebanon, Copernicus products seem to show more consistent estimates between Level 1 and 2, regardless of the model used, since the differences between ET rates are smaller and close to 0 mm/day, with the intraannual dekadal standard deviation more similar between scales. This is surprising, since Level 1 and Level 2 WaPOR products use the same thermal data (MODIS sensor) and may indicate the sensitivity of the ETLook contextual soil moisture retrieval method to differences in f_C obtained with different optical sensors (MODIS at Level 1 and PROBA-V at Level 2). In both Tunisia and Lebanon, the outputs produced by ETLook$_C$ clearly display the most scale consistency.

In the case of Lebanon, both Copernicus and WaPOR ET datasets are available for all three levels in the Bekaa Valley. As analogous to Tunisia, Fig. 11 shows the intercomparison of L3 against both L1 and L2 in the Bekaa Valley. Models using Copernicus data show no differences between Levels 3 and 2, since the 20-m ET was resampled to 100 m to obtain Level 2 data. On the other hand, WaPOR Level 2 yields significant lower ET estimates than Level 3 with also lower temporal variability, especially in irrigated agricultural areas.

VI. Discussion

A. Utility of Copernicus Data for ET Modeling

The results indicate the suitability of Copernicus data as inputs for consistent ET modeling at various spatial resolutions from 20 to 300 m. TSEB-PT$_C$ achieved correlation of 0.9 and bias of less than 0.3 mm/day when validating L3 ET against all the field measurements combined. The bias of both TSEB-PT$_C$ and ETLook$_C$ points to the underestimation of dekadal ET and it could partially be caused by the choice of the ET gap-filling method (see Section III-F and [28]). At the same time, both TSEB-PT$_C$ and ETLook$_C$ achieved a better accuracy than WaPOR at the one site where L2 ET was available from all three datasets (Tunisian rainfed olive grove). In addition, ETLook$_C$ performed the best when comparing consistency across the three spatial scales. While the validation sites represented a wide selection of irrigation practices and crop types, they are all located in semiarid Mediterranean climate. It could be argued that this represents the regions where irrigation demand is highest and water shortages most pressing. However, irrigation is being developed in countries as diverse as Uganda [39] and Denmark, and therefore, the validation effort should be extended to other climates. It should also be noted that WaPOR has to operate across all the African and Middle East climates, and while no climate or site specific adjustments were included in the preprocessing of Copernicus data or in modeling ET, some tradeoffs might be involved when the geographical area of interest is expanded.

The robustness of the LST sharpening approach for producing a high spatiotemporal resolution representation of the LST based on S3 observations is also demonstrated by the field validation results presented in Section V-A. ET derived with sharpened LST is well able to capture spatial and temporal patterns even of small fields with different irrigation and growing regimes compared to the neighboring parcels (e.g., potato and vineyard fields as shown in Fig. 2). However, those results also illustrate the limitation of sharpening low-resolution LST, namely the difficulty in capturing LST values that are outside of the range of the low-resolution LST, which by its nature is an aggregated value. This can be observed in the highest bias being present

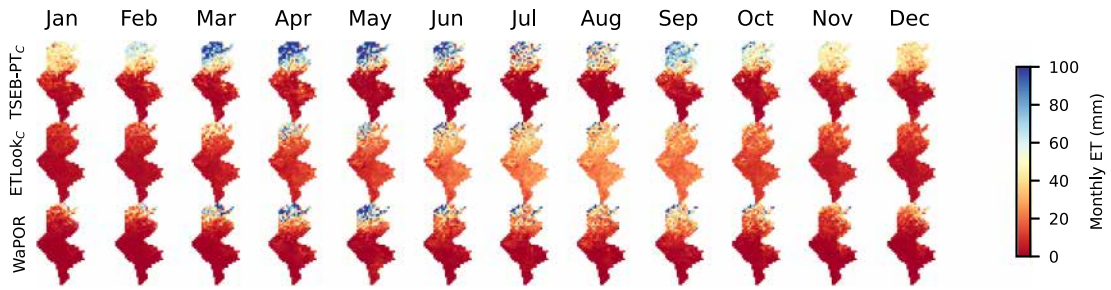

Fig. 7. Monthly cumulative ET maps for TSEB-PT$_C$ and ETLook$_C$ and WaPOR Level 2 (100 m) ET in Tunisia for year 2019. All maps share the same scale and colorbar.

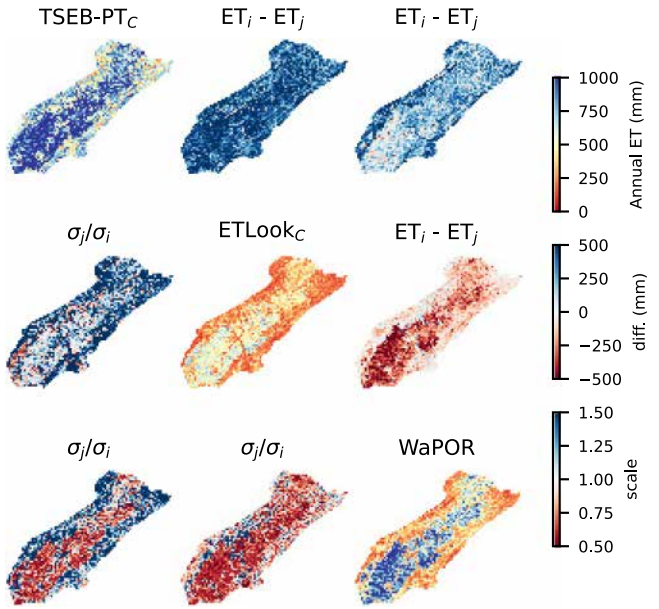

Fig. 8. Annual comparison of ET between WaPOR and Copernicus TSEB-PT and ETLook at Level 3 in the Bekaa Valley for year 2019. Maps in the diagonal show each model cumulative annual ET. The off-diagonal represents model intercomparison, both in ET differences (upper right) and in intraannual dekadal standard deviations scale (lower left). "*i*" represents the model sharing the row and "*j*" is the model sharing the column.

in the festuca site (well irrigated and surrounded by semiarid landscape) and was also reported in previous studies [8], [40]. While progressive enhancements to various LST sharpening methods are being proposed [40], [41], this issue cannot really be resolved without the use of thermal sensors with a high spatiotemporal resolution. In the context of Copernicus, this will be addressed by the proposed Land Surface Temperature Monitoring (LSTM) mission [42], which is planned with a 30–50 m spatial resolution, 1–3 days temporal resolution, and 1–1.5 K total uncertainty of the LST product, thus fulfilling the requirements for robust, field-scale monitoring of ET and water productivity [43]. In the meantime, a fusion between S3 and Landsat (high spatial but low temporal resolution) thermal observations could be explored, based on existing methods [44].

The meteorological forcing derived from ERA5 has the lowest original spatial resolution of all the input datasets, of around 30 km. We performed topographic corrections of these data through which the resolution is increased. To assess how this might impact local, parcel-scale ET estimates, we compared the orographic sharpened ERA5 fields against one meteorological station located in Bekaa valley, with results shown in Fig. 12 for reference ET (ET_{ref}). ET_{ref} combines all the relevant meteorological parameters needed for ET modeling and shows very high correlation and very low bias. Similar results have been obtained with other agrometeorological stations placed in areas outside the regions, which are the subject of this study (results, therefore, not shown), in which instantaneous air temperature and solar irradiance also corresponded well to ground measurements, while wind speed, which is the most difficult parameter to model at local scales, still showed acceptable results. This implies the suitability of ERA5 inputs even for high-resolution ET modeling. Copernicus CDS also provide access to ERA5-Land dataset, which contains only surface meteorological outputs of ERA5 but with a 9-km resolution [45]. It uses a conservative land mask that makes the use of this dataset impractical in coastal areas. However, in areas away from the coast, ERA5 Land might lead to even better agreement with local measurements. Finally, both ERA5 and ERA5-Land are distributed with a 3-month delay, due to stringent quality checks. However a dataset called ERA5T (T for preliminary Near Real Time) is distributed with a five-day delay and is also of very high quality. Therefore, ERA5 can be used for historical analysis, while ERA5T is available for near-real time processing.

Finally, the land-cover map can impact ET outputs through its influence on ancillary parameters such as vegetation height. CGLC has 23 land-cover classes, a high spatial resolution of 100 m, been updated annually since 2015, and was extensively validated resulting in an overall accuracy of 80% [46]. However, it still has some limitations when used in ET models. The first, particularly relevant for the SDG indicator 6.4.1 reporting in agriculture, is the presence of a single agricultural class. This class contains such diverse types as orchards, vineyards, and herbaceous annual crops, and all of them had to be assigned the same ancillary canopy parameters despite being clearly different. For example, in the approach used in this study, the vegetation height in agricultural pixels is scaled with LAI up to a maximum value of 1.5 m [9]. This results in the underestimation of the vegetation height in both the grapevine and young almond sites, while the overestimation is present in the potato and reference festuca sites. Olive grove location was classified as unknown forest type, and therefore, had a constant height of 1.5 m. In the TSEB-PT model, the underestimation of the

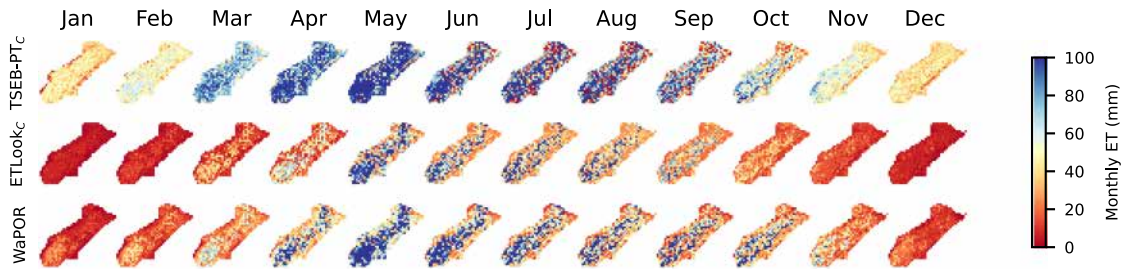

Fig. 9. Monthly cumulative ET maps for TSEB-PT$_C$ and ETLook$_C$ models using Copernicus Level 3 (20 m) data and WaPOR Level 3 (30 m) ET in Bekaa valley in Lebanon for year 2019. All maps share the same scale and colorbar.

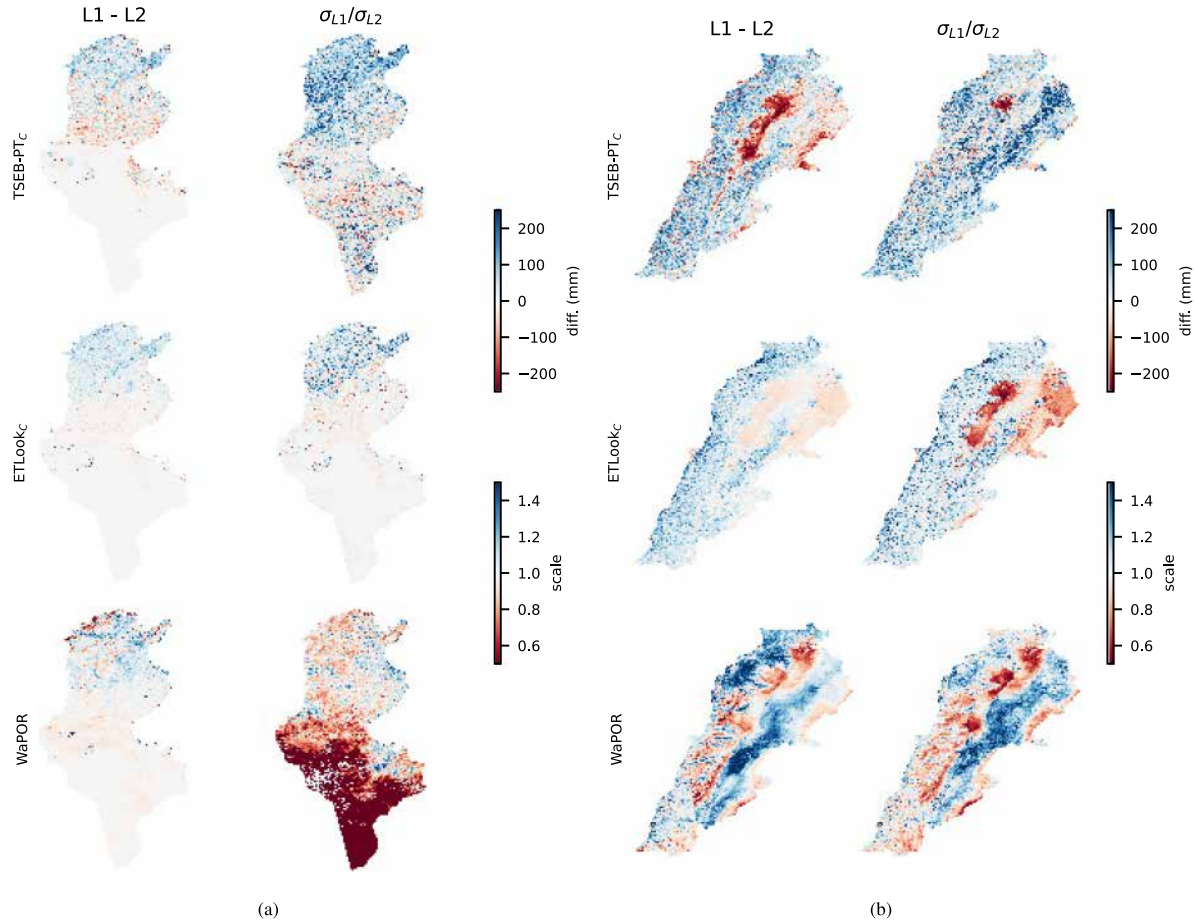

Fig. 10. Comparison of Levels 1 and 2 of Copernicus TSEB-PT$_C$, ETLook$_C$, and WaPOR ET products in (a) Tunisia and (b) Lebanon for year 2019. Left column of each panel shows the absolute difference in annual cumulative ET (diff. legend), while the right column shows the ratio between products in intra-annual dekadal variability of ET (scale legend). (a) Tunisia. (b) Lebanon.

vegetation height leads to potential underestimation of sensible heat flux (through the underestimation of surface roughness), and therefore, the overestimation of the latent heat flux, and vice versa. In Table IV, it can be seen that the largest underestimation of TSEB-PT$_C$ ET occurs in the festuca and potato sites, where the vegetation height is overestimated, and the largest overestimation of ET occurs in the grapevine site, where the vegetation height is underestimated. The second issue is the mismatch between CGLC spatial resolution and the 20-m S2 data used to set the output resolution of the Level 3 ET product. This results in visible 100 m by 100 m blocks in the output ET maps, especially apparent at the borders between two different land-cover classes, such as agriculture and forests. Landcover maps with a resolution of up to 10 m are being produced using Sentinel-2 data [47] and could potentially be used as inputs to ET modeling.

B. *Large-Scale Spatiotemporal ET Patterns*

Evaluating the large-scale spatiotemporal patterns of ET produced by the different model runs is more difficult and subjective, particularly since the differences between the data

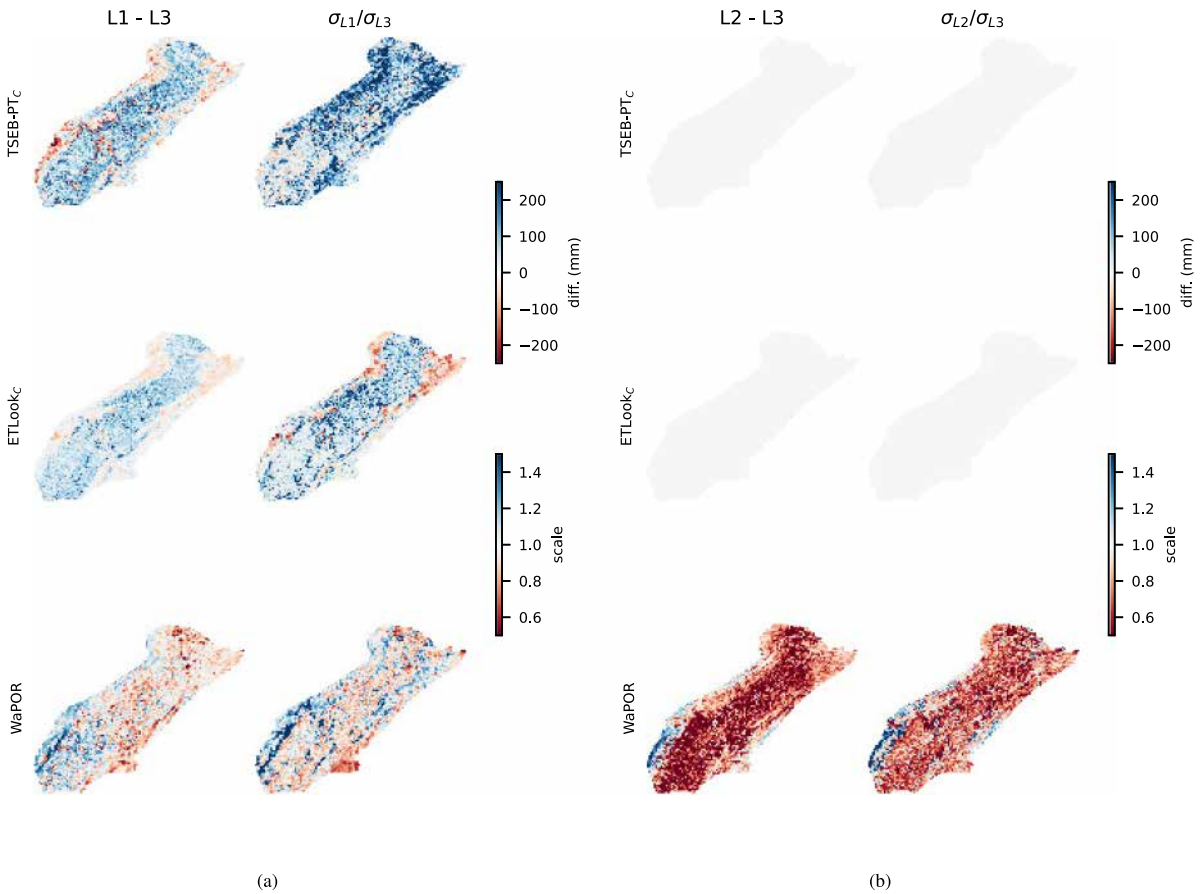

Fig. 11. Comparison of Levels 1 and 2 versus Level 3 for Copernicus TSEB-PT and ETLook and WaPOR ET products in Bekaa valley in Lebanon for year 2019. Left column of each panel shows the difference in annual sum of ET (diff. legend) and right column shows difference in dekadal intra-annual ET variability (scale legend). (a) L1 & L3. (b) L2 & L3.

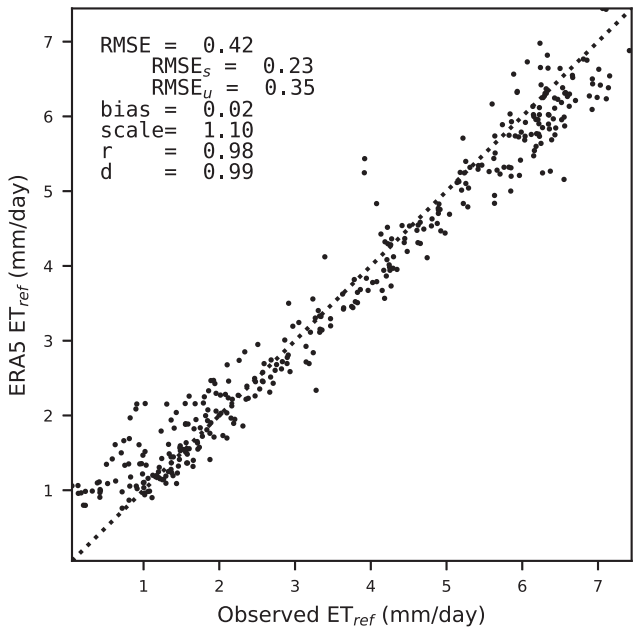

Fig. 12. Comparison of the daily reference ET modeled with topographically corrected ERA5 data against measurements in the Tal Amara station in Bekaa Valley.

sources (Copernicus and WaPOR inputs) are as significant as the differences between the ET models (TSEB-PT and ETLook). In general, TSEB-PT$_C$ tends to produce higher ET compared to ETLook, especially in vegetated areas, while WaPOR yields higher ET compared to ETLook$_C$. Temporal patterns are also complex with TSEB-PT$_C$ generally agreeing better with WaPOR in spring and summer, while ETLook$_C$ produces closer outputs to WaPOR in autumn and winter. At Level 2 (Tunisia and Fig. 6), TSEB-PT shows a larger range of ET values compared to ETLook, although WaPOR produces larger range in forested areas of northern Tunisia. At Level 3 (Bekaa valley and Fig. 8), TSEB-PT$_C$ still shows a larger range of values compared to ETLook$_C$ but in the irrigated cropland areas, the range produced by WaPOR is larger. At this spatial level, WaPOR uses Landsat LST, which, as discussed previously, has a larger dynamic range than the sharpened S3 LST, which leads to a larger range of ET values.

To help interpret the observed spatial patterns, we compared them against TerraClimate [48] actual ET and a CGLC map for year 2019 (see Fig. 13). TerraClimate dataset has a spatial resolution of ca. 4 km and temporal resolution of 1 month. It is based on a water-balance model forced with monthly reanalysis meteorological data and using as ancillary data climatic normals of land cover and phenology. The actual ET product is estimated

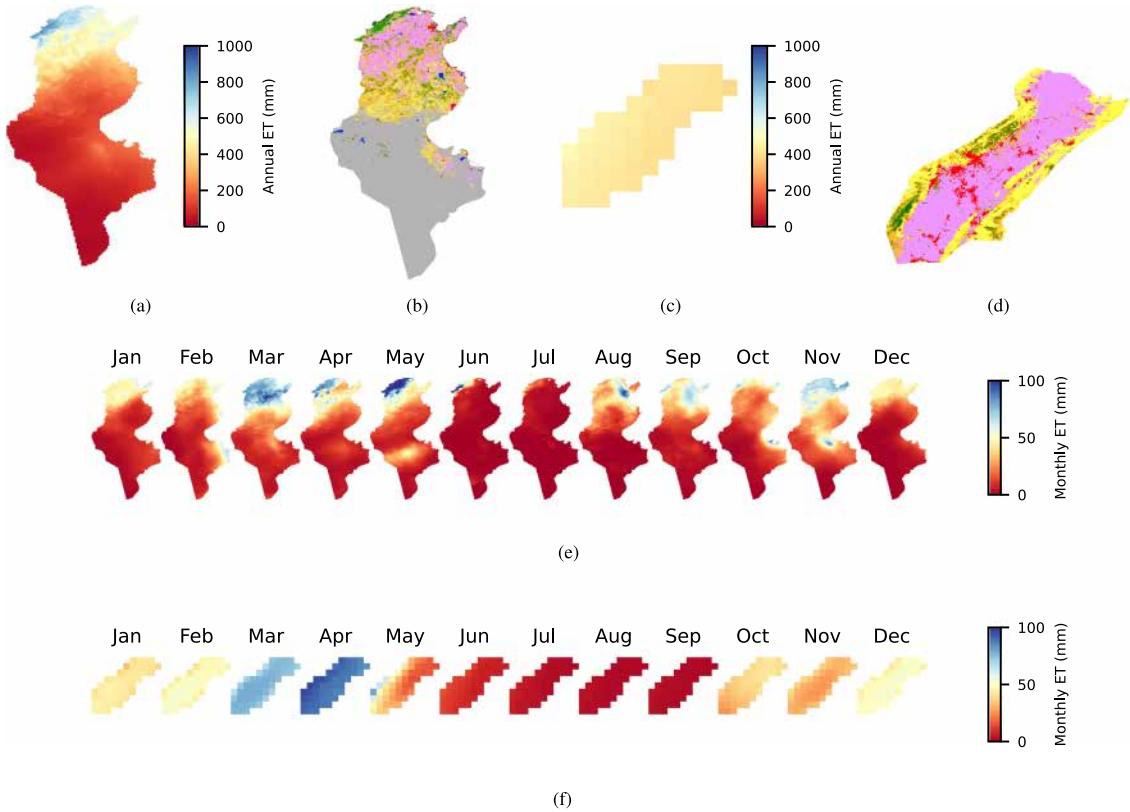

Fig. 13. TerraClimate actual monthly and annual ET and CGLC landcover map in Tunisia and Bekaa valley for year 2019. In CGLC map: agricultural areas are pink, urban areas are red, forests are green, grasslands are yellow, shrublands are orange, and bare areas are gray. (a) Annual ET Tunisia. (b) Land cover Tunisia. (c) Annual ET Bekaa. (d) Land cover Bekaa. (e) Monthly ET Tunisia. (f) Monthly ET Bekaa.

as reference ET constrained by available liquid and root-zone water with the root depth being time invariant and based on a map with a resolution of 0.5°. Therefore, it does not take into account parameters such as irrigation water input, variable root depth, vegetation height or functional type, etc. Nevertheless, it offers an independent comparison dataset and can be considered as minimum bound of the actual ET range based purely on meteorological variables such as rainfall, irradiance, and air temperature.

Considering the Tunisian annual ET [see Figs. 6 and 13(a)], ETLook$_C$ produces the closest spatial patterns and absolute values compared to TerraClimate, with ET of 600–800 mm/year on the north coast, around 500 mm/year in northern part of the country and 0–300 mm/year in the rest of Tunisia. The other two datasets produce generally higher ET in the north and lower ET in the barren and desert southern areas compared to TerraClimate. WaPOR dataset has clearly higher ET values in areas classified as forests in CGLC, while TSEB-PT$_C$ has equally high ET in forested and agricultural areas of northern Tunisia. This could be due to the influence of landcover map on ET models, in particular, vegetation height, but also due to geography with forests being mostly located in mountainous areas and agriculture placed in areas classified as temperate or arid-steppe by the Köppen–Geiger classification and rest of Tunisia being classified as arid desert. In Bekaa valley, TerraClimate is much lower than the three EO-based datasets due to not accounting for irrigation, which is widely used in this area. Outside of agricultural areas, TSEB-PT$_C$ produces higher ET and both ETLook datasets produce lower ET than TerraClimate. All the models capture the agricultural areas, although with large differences in the absolute ET values.

In addition, the effect of irrigation and land cover/land use can be observed when comparing the monthly trends between TerraClimate and the EO-based models. TerraClimate yields ET rates closer to zero during the late spring and summer months (i.e., May to September) in the Bekaa Valley as compared to the EO-based models [see Figs. 9 and 13(f)]. Considering this area as intensively irrigated, thanks to the snowmelt and the existing reservoir infrastructure, one could assume that the EO-based models provide a more reliable estimate of water use than TerraClimate during this season. Similar spatiotemporal disagreement is found in the monthly trends for Tunisia [see Figs. 7 and 13(e)], which is evident in the northern part where most of the croplands are located [see Fig. 13(b)] during June and July. Based on the observations made before, we could hypothesize that these differences are also due to irrigation practices in the country during the dry season. Indeed, according to the FAO, 455 070 ha were accounted as irrigated land in Tunisia,[7] which approximately correspond (making use of the

[7][Online]. Available: http://www.fao.org/aquastat/en/geospatial-information/global-maps-irrigated-areas/irrigation-by-country/country/TUN, last visited 11.06.2021

CGLC map of Fig. 13(b)) to ca. 25% of the total agricultural land.

C. Ensuring Consistency Between Spatial Scales

An important aspect when estimating ET at multiple spatial scales is to ensure consistency across those scales. This is important from a theoretical point of view because mass and energy should be conserved, and from a practical point of view because regional or national estimates of water use should not change depending the spatial resolution of the map that is being used. In the datasets produced in this study (TSEB-PT$_C$ and ETLook$_C$), we tried to achieve this consistency by utilizing the same data across all spatial scales (including thermal data), apart from shortwave optical that came from S3 observations at L1 and S2 observations at L2 and L3. In addition, we ensured conservation of thermal energy when sharpening LST between the different resolutions and developed a method to ensure consistency between biophysical parameters derived from S2 and S3 L2A products (see Section III-D). Finally, since Copernicus-based L2 and L3 ET is based on exactly the same inputs, we resampled the output of L3 processing to obtain L2 ET instead of resampling the model inputs. When compared to WaPOR ET maps, which rely on different satellite data at all three levels, the Copernicus-based ETLook ET maps do provide improved consistency across all levels (see Figs. 10 and 11).

However, some differences remain between L1 and other levels even for ETLook$_C$ and TSEB-PT$_C$ datasets. Those differences can be attributed to two main factors. First, both TSEB-PT and ETLook models depend on the landcover map for setting ancillary parameters (see Table III) and that landcover map is aggregated to the coarser resolution using the statistical mode of the discrete land cover classes. This means that, e.g., a patchwork of urban and agricultural pixels at L3 might become an urban pixel at L1. The TSEB-PT model is more sensitive to those ancillary parameters compared to ETLook (especially to the canopy height), and thus, the differences between L1 and other levels are larger for TSEB-PT$_C$ ET outputs (see Figs. 10 and 11). A possible solution could be to first produce maps of ancillary parameters at the highest spatial resolution before aggregating them using averaging to the lower resolutions. The second factor, is the models' assumption of subpixel homogeneity that can produce increased output uncertainty in environments in which subpixel heterogeneity is present [38], [49]. This assumption becomes increasingly less valid as the pixel size increases. This is a more complex issue to solve and could require a change of paradigm of ET model assumptions.

D. Evaluation of WaPOR ET

The model used in WaPOR ET, ETLook, is rather recent having been published in 2012 [10], and therefore, there are few studies validating its performance. On the other hand, the first version of TSEB-PT was published in 1995 [50], and hence, it has been applied and validated at a larger number of studies and in different environments (e.g., [9], [11], [51], and[52]). Nevertheless, ETLook has shown its potential in tracking the spatiotemporal variability of ET, with a correlation coefficient between the observed and the predicted of 0.9 in this study, which is consistent with the findings of the previous study that showed an R^2 of 0.54 (equivalent to a correlation of 0.73) for a larger number of study sites [53]. However, the *in situ* validation in this study showed that ETLook$_C$ systematically underestimated dekadal ET in irrigated and rainfed semiarid croplands, and also tended to yield lower cumulative monthly and annual ET rates as compared to the TSEB-PT$_C$ model. Significant biases for the WaPOR ET product in semiarid rainfed croplands were also found in [53], with relative errors higher than 50% of the measured dekadal ET rates. The same study also showed that the WaPOR product tends to overestimate the ET at irrigated croplands, which is the opposite to results in our study in the Barrax sites. However, we run ETLook at those sites using Copernicus inputs instead of WaPOR-like inputs. Furthermore, the authors in [54] also pointed out the trend of WaPOR underestimating ET as compared to lysimeter measurements in an alfalfa field in Iran.

Regarding the spatial consistency between levels, behavior similar to what was found in this study has also been observed in previous studies [53], [55], with WaPOR L3 yielding largest ET annual and monthly trends as compared to L1 and L2. The authors of these two studies also pointed out the effect of using PROBA-V for L2 (100 m) ET after 2014 (MODIS was used previously), which led to a loss of consistency against L1 (300 m). In this study, we proposed a method for ensuring the spatial consistency across scales (see Section III-D), which minimized such disagreements of water accounting at different spatial resolutions. This relied in part on limiting the number of satellite sensors used within the ET modeling scheme. However, this presents a tradeoff between using limited datasets and using data at the most appropriate spatial resolution, as illustrated by using sharpened SLSTR thermal data (due to present lack of the Copernicus high-spatial thermal infrared mission), which might lead to larger uncertainties in tracking either stress or wetting events in the shorter term.

VII. Conclusion

Estimating spatial and temporal patterns of ET is essential for accurate reporting of the agricultural component of the SDG target 6.4. The use of Earth-observation-based ET estimates can improve the consistency of this reporting across administrative and natural boundaries, thus increasing transparency and trust. In this study, we evaluated whether Copernicus products are suitable as input datasets for ET models. The ET product available on the WaPOR portal, run by the FAO with the aim of encouraging the use of satellite observations in SDG 6.4 reporting, was used as a benchmark. Therefore, we assessed the accuracy, consistency, and spatial patterns of Copernicus-based ET at 10-day timestep and three spatial resolutions (20, 100, and 300 m).

The results from validating the estimated Copernicus-based ET against measurements from six field sites spread across irrigated and rainfed agriculture in semiarid Mediterranean climate indicate a mean bias of less than 0.3 mm/day using the TSEB-PT model. At the same time, when Copernicus inputs are

used with the same ET model as used in WaPOR (ETLook), a better consistency across spatial scales is obtained compared to WaPOR. This is due to limiting the number of different satellite sensors when modeling at different spatial resolutions and the use of inputs' preprocessing methods designed to ensure consistency. Large-scale spatiotemporal patterns resulting from monthly and annual aggregations of the different ET products are more difficult to interpret, although the models do show the same general outlines and spatiotemporal trends consistent with irrigation patterns, as opposed to model purely driven with meteorological forcing.

Although the results show high suitability of Copernicus-based ET for SDG reporting, a number of issues should be addressed to further increase the quality of the outputs. Some of them can be addressed in the shorter term, while others require a long-term perspective. Among the former, is the fact that the ET model that produced the most accurate fluxes (TSEB-PT) was also less consistent across spatial scales compared to the model used in WAPOR (ETLook). This is mainly due to its sensitivity to land-cover-based parameters and might require a modification to the preprocessing of model input data or including additional remote sensing data with information on canopy structure such as SAR and/or LiDAR. Second, the validation should be extended to other climatic zones. Even though the Mediterranean region has among highest proportion of freshwater withdrawals used in the irrigated agriculture in the world, irrigation is widely used across the globe. An issue that requires a longer term perspective is the lack of a high spatiotemporal resolution thermal sensor within the Copernicus constellation. A Copernicus LSTM mission addressing this data gap is being planned but it will not be operational for many years yet. In the meantime, advanced data fusion methods between different satellite sensors can partially fill this gap.

In summary, this study has demonstrated that products based on satellite observations and meteorological models made freely and openly available by the Copernicus program are highly suitable for consistent and robust estimation of ET in the context of SDG reporting. By relying on predominantly Copernicus data, it is possible to take advantage of its operational data quality and guaranteed long-term continuity, thus laying a robust baseline for monitoring of changes in the SDG 6.4 indicators.

ACKNOWLEDGMENT

The authors would like to thank FAO for providing technical and theoretical advice. In particular, the authors would like to thank ESA's B. Koetz and FAO's L. Peiser and J. Hoogeveen for regular discussions and feedback. The authors would also like to thank J. González-Piqueras who is responsible for the wheat EC tower and the collaborators in Lebanon, Tunisia, and Spain.

REFERENCES

[1] M. Paganini *et al.*, *Satellite Earth Observations in Support of the Sustainable Development Goals: The CEOS Earth Observation Handbook* (Special 2018 ed.). Paris, France: The Committee on Earth Observation Satellites and the European Space Agency, 2018. [Online]. Available: http://eohandbook.com/sdg/files/CEOS_EOHB_2018_SDG.pdf

[2] Group on Earth Observations, "EO4SDG: Earth observations in service of the 2030 agenda for sustainable development, Strategic Implementation Plan 2020–2024," *Group on Earth Observations*, Geneva, Switzerland, Tech. Rep., 2019. [Online]. Available: https://earthobservations.org/documents/gwp20_22/eo_for_sustainable_development_goals_ip.pdf

[3] B. O'Connor *et al.*, *Compendium of Earth Observation Contributions to the SDG Targets and Indicators*. Paris, France: European Space Agency, May 2020. [Online]. Available: https://eo4society.esa.int/wp-content/uploads/2021/01/EO_Compendium-for-SDGs.pdf

[4] UN Water, "Step-by-step methodology for monitoring water use efficiency (*6.4.1*)," UN Water, Geneva, Switzerland, Tech. Rep., Jul. 2019. [Online]. Available: https://www.unwater.org/publications/step-step-methodology-monitoring-water-use-efficiency-6-4-1/

[5] UN Water, "Step-by-step methodology for monitoring water stress (*6.4.2*)," UN Water, Geneva, Switzerland, Tech. Rep., Feb. 2019. [Online]. Available: https://www.unwater.org/publications/step-step-methodology-monitoring-water-stress-6-4-2/

[6] AQUASTAT-FAO, "FAO's information system on water and agriculture," Food and Agriculture Organization of the United Nations, Rome, Tech. Rep., 2018. [Online]. Available: http://www.fao.org/aquastat/en/

[7] FRAME Consortium, WaPOR Data Manual—Evapotranspiration v2, Jun. 2020. [Online]. Available: https://bitbucket.org/cioapps/wapor-et-look/downloads/FRAME_ET_v2_data_manual_finaldraft_v2.2.pdf

[8] R. Guzinski and H. Nieto, "Evaluating the feasibility of using Sentinel-2 and Sentinel-3 satellites for high-resolution evapotranspiration estimations," *Remote Sens. Environ.*, vol. 221, pp. 157–172, Feb. 2019. [Online]. Available: http://www.sciencedirect.com/science/article/pii/S0034425718305285

[9] R.H. Guzinski, I. NietoSandholt, and G. Karamitilios, "Modelling high-resolution actual evapotranspiration through Sentinel-2 and Sentinel-3 data fusion," *Remote Sens.*, vol. 12, no. 9, p. 1433, Jan. 2020. [Online]. Available: https://www.mdpi.com/2072-4292/12/9/1433

[10] W. G. M. Bastiaanssen, M. J. M. Cheema, W. W. Immerzeel, I. J. Miltenburg, and H. Pelgrum, "Surface energy balance and actual evapotranspiration of the transboundary Indus basin estimated from satellite measurements and the ETLook model," *Water Resour. Res.*, vol. 48, no. 11, 2012. [Online]. Available: https://agupubs.onlinelibrary.wiley.com/doi/abs/10.1029/2011WR010482

[11] W. P. Kustas *et al.*, "*Revisiting the paper*, Using radiometric surface temperature for surface energy flux estimation in mediterranean drylands from a two-source perspective," *Remote Sens. Environ.*, vol. 184, pp. 645–653, Oct. 2016. [Online]. Available: http://www.sciencedirect.com/science/article/pii/S0034425716302814

[12] J. L. Monteith, "Evaporation and environment," in *Symposia of the Society for Experimental Biology*. Cambridge, U.K.: Cambridge Univ. Press, vol. 19, 1965, pp. 205–234. [Online]. Available: https://repository.rothamsted.ac.uk/item/8v5v7/evaporation-and-environment

[13] Jarvis, "The interpretation of the variations in leaf water potential and stomatal conductance found in canopies in the field," *Philos. Trans. Roy. Soc. London, B. Biol. Sci.*, vol. 273, no. 927, pp. 593–610, Feb. 1976. [Online]. Available: https://royalsocietypublishing.org/doi/10.1098/rstb.1976.0035

[14] Y. Yang *et al.*, "Estimation of surface soil moisture from thermal infrared remote sensing using an improved trapezoid method," *Remote Sens.*, vol. 7, no. 7, pp. 8250–8270, Jul. 2015. [Online]. Available: https://www.mdpi.com/2072-4292/7/7/8250

[15] H. Hersbach *et al.*, "The ERA5 global reanalysis," *Quart. J. Roy. Meteorological Soc.*, vol. 146, no. 730, pp. 1999–2049, 2020. [Online]. Available: https://rmets.onlinelibrary.wiley.com/doi/abs/10.1002/qj.3803

[16] N. M. SissenwineDubin, and H. Wexler, "The U.S. Standard Atmosphere, 1962," *J. Geophys. Res.*, vol. 67, no. 9, pp. 3627–3630, 1962. [Online]. Available: https://agupubs.onlinelibrary.wiley.com/doi/abs/10.1029/JZ067i009p03627

[17] *P. Ineichen*, "A broadband simplified version of the Solis clear sky model," *Sol. Energy*, vol. 82, no. 8, pp. 758–762, Aug. 2008. [Online]. Available: https://www.sciencedirect.com/science/article/pii/S0038092X08000406

[18] C. J. Aguilar Herrero and M. J. Polo, "Topographic effects on solar radiation distribution in mountainous watersheds and their influence on reference evapotranspiration estimates at watershed scale," *Hydrol. Earth Syst. Sci.*, vol. 14, no. 12, pp. 2479–2494, Dec. 2010. [Online]. Available: https://www.hydrol-earth-syst-sci.net/14/2479/2010/

[19] G. A. Allen, L. S. Pereira, and D. Raes, "Crop evapotranspiration: guidelines for computing crop water requirements," *FAO Irrigation and Drainage Paper*, 1998. [Online]. Available: https://agris.fao.org/agris-search/search.do?recordID=SO2005100020

[20] M. Drusch *et al.*, "Sentinel-2: ESA's optical high-resolution mission for GMES operational services," *Remote Sens. Environ.*, vol. 120, pp. 25–36, May 2012. [Online]. Available: http://www.sciencedirect.com/science/article/pii/S0034425712000636

[21] M. Main-Knorn *et al.*, "Sen2Cor for sentinel-2," in *Proc. Image Signal Process. Remote Sensing XXIII*, Oct. 2017, vol. 10427, Art. no. 1042704. [Online]. Available: https://www.spiedigitallibrary.org/conference-proceedings-of-spie/10427/1042704/Sen2Cor-for-Sentinel-2/10.1117/12.2278218.short

[22] D. E. Frantz A. Haß J. UhlStoffels, and J. Hill, "Improvement of the Fmask algorithm for Sentinel-2 images: Separating clouds from bright surfaces based on parallax effects," *Remote Sens. Environ.*, vol. 215, pp. 471–481, Sep. 2018. [Online]. Available: http://www.sciencedirect.com/science/article/pii/S0034425718302037

[23] C. Donlon *et al.*, "The global monitoring for environment and security (GMES) Sentinel-3 mission," *Remote Sens. Environ.*, vol. 120, pp. 37–57, May 2012. [Online]. Available: http://www.sciencedirect.com/science/article/pii/S0034425712000685

[24] G. S.Campbell, "Extinction coefficients for radiation in plant canopies calculated using an ellipsoidal inclination angle distribution," *Agricultural Forest Meteorol.*, vol. 36, no. 4, pp. 317–321, Apr. 1986. [Online]. Available: https://www.sciencedirect.com/science/article/pii/0168192386900109

[25] E. F. Vermote, D. Tanre, J. L. Deuze, M. Herman, and J. Morcette, "Second simulation of the satellite signal in the solar spectrum 6S: An overview," *IEEE Trans. Geosci. Remote Sens.*, vol. 35, no. 3, pp. 675–686, May 1997.

[26] F.W. P. GaoKustas, and M. C. Anderson, "A data mining approach for sharpening thermal satellite imagery over land," *Remote Sens.*, vol. 4, no. 11, pp. 3287–3319, Oct. 2012. [Online]. Available: http://www.mdpi.com/2072-4292/4/11/3287

[27] C. Cammalleri, M. C. Anderson, and W. P. Kustas, "Upscaling of evapotranspiration fluxes from instantaneous to daytime scales for thermal remote sensing applications," *Hydrol. Earth Syst. Sci.*, vol. 18, no. 5, pp. 1885–1894, 2014. [Online]. Available: https://hess.copernicus.org/articles/18/1885/2014/

[28] E. Delogu, A. Olioso, A. Alliès, J. Demarty, and G. Boulet, "Evaluation of multiple methods for the production of continuous evapotranspiration estimates from TIR remote sensing," *Remote Sens.*, vol. 13, no. 6, Jan. 2021, Art. no. 1086. [Online]. Available: https://www.mdpi.com/2072-4292/13/6/1086

[29] T. Twine *et al.*, "Correcting eddy-covariance flux underestimates over a grassland," *Agricultural Forest Meteorol.*, vol. 103, no. 3, pp. 279–300, 2000.

[30] W. Chebbi *et al.*, "Analysis of evapotranspiration components of a rainfed olive orchard during three contrasting years in a semi-arid climate," *Agricultural Forest Meteorol.*, vol. 256–257, pp. 159–178, 2018.

[31] D. Vitale, G. Fratini, M. Bilancia, G. Nicolini, S. Sabbatini, and D. Papale, "A robust data cleaning procedure for eddy covariance flux measurements," *Biogeosciences*, vol. 17, no. 6, pp. 1367–1391, 2020.

[32] R. López-Urrea *et al.*, "Evapotranspiration and crop coefficients of irrigated biomass sorghum for energy production," *Irrigation Sci.*, vol. 34, no. 4, pp. 287–296, Jul. 2016. [Online]. Available: https://doi.org/10.1007/s00271-016-0503-y

[33] L. Pereira, P. Paredes, D. Hunsaker, R. López-Urrea, and N. Jovanovic, "Updates and advances to the FAO56 crop water requirements method," *Agricultural Water Manage.*, vol. 248, Apr. 2021, Art. no. 106697.

[34] R. López-Urrea, F. Martín de Santa Olalla, C. Fabeiro, and A. Moratalla, "Testing evapotranspiration equations using lysimeter observations in a semiarid climate," *Agricultural Water Manage.*, vol. 85, no. 1, pp. 15–26, 2006.

[35] J. M. Sánchez, R. López-Urrea, F. Valentín, V. Caselles, and J. M. Galve, "Lysimeter assessment of the simplified two-source energy balance model and eddy covariance system to estimate vineyard evapotranspiration," *Agricultural Forest Meteorol.*, vol. 274, pp. 172–183, 2019.

[36] J. M. Sánchez, L. Simón, J. González-Piqueras, F. Montoya, and R. López-Urrea, "Monitoring crop evapotranspiration and transpiration/evaporation partitioning in a drip-irrigated young almond orchard applying a two-source surface energy balance model," *Water*, vol. 13, no. 15, p. 2073, Jan. 2021. [Online]. Available: https://www.mdpi.com/2073-4441/13/15/2073

[37] C. J. Willmott, "Some comments on the evaluation of model performance," *Bull. Amer. Meteorological Soc.*, vol. 63, no. 11, pp. 1309–1313, 1982.

[38] V. Burchard-Levine *et al.*, "The effect of pixel heterogeneity for remote sensing based retrievals of evapotranspiration in a semi-arid tree-grass ecosystem," *Remote Sens. Environ.*, vol. 260, Jul. 2021, Art. no. 112440. [Online]. Available: https://www.sciencedirect.com/science/article/pii/S0034425721001589

[39] W. Joshua *et al.*, "Irrigation development in Uganda: Constraints, lessons learned, and future perspectives," *J. Irrigation Drainage Eng.*, vol. 143, no. 5, May 2017, Art. no. 04017003. [Online]. Available: https://ascelibrary.org/doi/abs/10.1061/(ASCE)IR.1943-4774.0001159

[40] J. M. Sánchez *et al.*, "Monitoring 10-m LST from the combination MODIS/Sentinel-2, validation in a high contrast semi-arid agroecosystem," *Remote Sens.*, vol. 12, no. 9, p. 1453, Jan. 2020. [Online]. Available: https://www.mdpi.com/2072-4292/12/9/1453

[41] S. M. Njuki, C. M. Mannaerts, and Z. Su, "An improved approach for downscaling coarse-resolution thermal data by minimizing the spatial averaging biases in random forest," *Remote Sens.*, vol. 12, no. 21, p. 3507, Jan. 2020. [Online]. Available: https://www.mdpi.com/2072-4292/12/21/3507

[42] B. Koetz *et al.*, "High spatio-temporal resolution land surface temperature mission—A copernicus candidate mission in support of agricultural monitoring," in *Proc. IEEE Int. Geosci. Remote Sens. Symp.*, Jul. 2018, pp. 8160–8162.

[43] B. Koetz *et al.*, "Copernicus high spatio-temporal resolution land surface temperature mission: Mission requirements document," European Space Agency, The Netherlands, Tech. Rep. Revision 3, May 2021. [Online]. Available: https://esamultimedia.esa.int/docs/EarthObservation/Copernicus_LSTM_MRD_v3.0_Issued_20210514.pdf

[44] K. R. Knipper *et al.*, "Using high-spatiotemporal thermal satellite ET retrievals to monitor water use over California vineyards of different climate, vine variety and trellis design," *Agricultural Water Manage.*, vol. 241, Nov. 2020, Art. no. 106361. [Online]. Available: http://www.sciencedirect.com/science/article/pii/S0378377420305473

[45] J. Muñoz *et al.*, "ERA5-Land: A state-of-the-art global reanalysis dataset for land applications," *Earth Syst. Sci. Data Discuss.*, pp. 1–50, Mar. 2021. [Online]. Available: https://essd.copernicus.org/preprints/essd-2021-82/

[46] N.-E. Tsendbazar *et al.*, "Copernicus global land service: Land cover 100 m: Version 3 globe 2015–2019: Validation report," Zenodo, Geneve, Switzerland, Tech. Rep., Sep. 2020. [Online]. Available: https://zenodo.org/record/4723975#.YLR1cKF8LmE

[47] R. Malinowski *et al.*, "Automated production of a land cover/use map of Europe based on Sentinel-2 imagery," *Remote Sens.*, vol. 12, no. 21, Jan. 2020, Art. no. 3523. [Online]. Available: https://www.mdpi.com/2072-4292/12/21/3523

[48] J. T. Abatzoglou, S. Z. Dobrowski, S. A. Parks, and K. C. Hegewisch, "TerraClimate, a high-resolution global dataset of monthly climate and climatic water balance from 1958–2015," *Sci. Data*, vol. 5, no. 1, Jan. 2018, Art. no. 170191. [Online]. Available: https://www.nature.com/articles/sdata2017191

[49] A. Nassar *et al.*, "Influence of model grid size on the estimation of surface fluxes using the two source energy balance model and sUAS imagery in Vineyards," *Remote Sens.*, vol. 12, no. 3, p. 342, Jan. 2020. [Online]. Available: https://www.mdpi.com/2072-4292/12/3/342

[50] J.W. NormanKustas, and K. Humes, "Source approach for estimating soil and vegetation energy fluxes in observations of directional radiometric surface temperature," *Agricultural Forest Meteorol.*, vol. 77, no. 3, pp. 263–293, 1995. [Online]. Available: https://www.sciencedirect.com/science/article/pii/016819239502265Y

[51] J. Cristo'bal *et al.*, "Surface energy flux estimation in two Boreal settings in Alaska using a thermal-based remote sensing model," *Remote Sens.*, vol. 12, no. 24, Jan. 2020, Art. no. 4108. [Online]. Available: https://www.mdpi.com/2072-4292/12/24/4108

[52] Y. Li *et al.*, "Evapotranspiration partitioning at field scales using TSEB and multi-satellite data fusion in the middle reaches of Heihe River Basin, Northwest China," *Remote Sens.*, vol. 12, no. 19, Jan. 2020, Art. no. 3223. [Online]. Available: https://www.mdpi.com/2072-4292/12/19/3223

[53] M. L. Blatchford *et al.*, "Evaluation of wapor v2 evapotranspiration products across Africa," *Hydrological Processes*, vol. 34, no. 15, pp. 3200–3221, 2020. [Online]. Available: https://onlinelibrary.wiley.com/doi/abs/10.1002/hyp.13791

[54] M.A. Javadian, M. Behrangi,Gholizadeh, and M. Tajrishy, "Metric and wapor estimates of evapotranspiration over the lake Urmia Basin: Comparative analysis and composite assessment," *Water*, vol. 11, no. 8, 2019. [Online]. Available: https://www.mdpi.com/2073-4441/11/8/1647

[55] M. Blatchford, C. M. Mannaerts, Y. Zeng, H. Nouri, and P. Karimi, "Influence of spatial resolution on remote sensing-based irrigation performance assessment using wapor data," *Remote Sens.*, vol. 12, no. 18, 2020. [Online]. Available: https://www.mdpi.com/2072-4292/12/18/2949

Radoslaw Guzinski received the B.Eng. (Hons.) degree in computer systems engineering from the University of Adelaide, Adelaide, Australia, in 2005, the M.Sc. degree in physical geography and ecosystem modeling from Lund University, Lund, Sweden, in 2010, and the Ph.D. degree with the focus on estimating of evapotranspiration at different scales using MODIS and Landsat data from the University of Copenhagen, Copenhagen, Denmark, in 2014.

He has more than ten years research experience in satellite-based modeling of evapotranspiration at various spatial scales. He started his career as a Software Engineer. During a Research Fellowship with ESA Centre for Earth Observation—ESRIN (2017–2018), he started developing methods for fusing Sentinel-2 and Sentinel-3 observations with the aim of deriving daily ET at 20-m resolution. He is currently with DHI GRAS (dhi-gras.com), where he focuses on applications in the domains of agriculture and water management and leads development of physically based models and machine-learning methods utilizing remotely sensed data.

Hector Nieto received the Ph.D. degree on Remote Sensing, Cartography and GIS from the University of Alcalá, Alcalá de Henares, Spain, in 2010.

He is currently with COMPLUTIG SL, a technology-based company, University of Alcalá. He has authored and co-authored more than 60 scientific publications in peer-reviewed journals and also a provider of open-source code for either scientific or commercial usage. Most of his scientific career has been developed with the University of Copenhagen, USDA Agricultural Research Service and Spanish Research Council. His research interests include the use of remote sensing for monitoring evapotranspiration and crop water stress at different spatiotemporal scales.

Juan Manuel Sánchez received the B.Sc., M.Sc., and Ph.D. degrees in physics from the University of Valencia, Valencia, Spain, in 2003, 2005, and 2008, respectively.

He is currently an Associate Professor with the Applied Physics Department, and a Researcher with the Regional Development Institute, University of Castilla-La Mancha, Ciudad Real, Spain. He has authored/co-authored about 50 papers in journals indexed in JCR, six book chapters, and more than 100 conference papers and has participated in 25 international, national, and regional projects, and is also a Referee in 18 international journals. His research interests include thermal infrared remote sensing in general and the surface energy balance in particular.

Dr. Sánchez was the recipient of the Nobert Gerbier-MUMM Internatinal Award 2010 by the World Meteorological Organization.

Ramón López-Urrea received the B.Sc., M.Sc., and Ph.D. degrees in agricultural engineering from Castilla-La Mancha University, Ciudad Real, Spain, in 1997, 1999, and 2004, respectively.

He is currently a Research Scientist with the Water Management Research Unit, Technical Institute of Agronomy for Albacete province, Albacete, Spain. He has authored/co-authored 42 papers in journals indexed in ISI-JCR, ten book chapters, and 97 conference papers. He has participated in 20 national and international projects. The mid-to-long term scientific-technical interests and objectives of his research are: to deepen in the knowledge of crop water requirements under a climate change scenario, through different approaches (lysimetry, micrometeorology, remote sensing, etc.), as well as, to evaluate different irrigation strategies aimed to mitigate the negative effects of water stress in crops.

Dr. López-Urrea has been an Associate Editor for the scientific journal *Irrigation Science* since July 2018.

Dalenda Mahjoub Boujnah received the Ph.D. degree in applied agronomic and biological sciences from the Faculty of Bioengineering, Department of Ecology, Gent University, Belgium, in 1996.

She is currently a Professor in ecophysiology with Research and Higher Education Agricultural Institution Tunisia, Olive Tree Institute, Sousse, Tunisia, and a Member of the Laboratory "Sustainability of the Olive Tree in Semiarid and Arid Climate of Tunisia-(R16IO 02)" under the authority of the Ministry of Higher Education and Scientific Research.

Gilles Boulet received an "Habilitation" (tenure) degree in space hydrology from Université Toulouse, France and the Ph.D. degree in hydrology from Université Grenoble, France.

He is an IRD Senior Researcher with CESBIO, Toulouse, France. He leads the Ecosystem Stress Scientific Committee on the French side of the joint Indo-French TRISHNA Thermal Infra Red mission proposal and has lead several projects sponsored by the French Space Agency to develop and evaluate ET products based on remote sensing data. He has more than 25 years of experience in field experiments and research developments focusing on applications for sustainable management of agricultural water. He currently leads one of the two CESBIO research teams entitled "Modelling and remote sensing of land surface processes" and is the Deputy Head for Science of the Midi-Pyrénées Observatory. He has authored and coauthored about 100 papers in peer referred journals and his h-index is 29. His research interests include evapotranspi ration retrieval from thermal infrared data, land surface process modeling, and data assimilation.